

Measuring galaxy abundance and clustering at high redshift from incomplete spectroscopic data: Tests on mock catalogs and application to zCOSMOS

Jiacheng Meng^{1*}, Cheng Li^{1†}, H.J. Mo², Yangyao Chen^{1,2}, Kai Wang^{1,2}

¹*Department of Astronomy, Tsinghua University, Beijing 100084, China*

²*Department of Astronomy, University of Massachusetts Amherst, MA 01003, USA*

Accepted XXX. Received YYY; in original form ZZZ

ABSTRACT

The number density and correlation function of galaxies are two key quantities to characterize the distribution of the observed galaxy population. High- z spectroscopic surveys, which usually involve complex target selection and are incomplete in redshift sampling, present both opportunities and challenges to measure these quantities reliably in the high- z Universe. Using realistic mock catalogs we show that target selection and redshift incompleteness can lead to significantly biased results. We develop methods to correct such bias, using information provided by the parent photometric data from which the spectroscopic sample is constructed. Our tests using realistic mock samples show that our methods are able to reproduce the true stellar mass function and correlation function reliably. As applications, mock catalogs are constructed for two high- z surveys: the existing zCOSMOS-bright galaxy sample and the forthcoming PFS galaxy evolution survey. We apply our methods to the zCOSMOS-bright sample and make comparisons with results obtained before. The same set of mock samples are used to quantify cosmic variances expected for different sample sizes. We find that, for both number density and correlation function, the relative error due to cosmic variance in the PFS galaxy survey will be reduced by a factor of 3-4 when compared to zCOSMOS.

Key words: mock catalogs – galaxies: high redshift – galaxies: luminosity function, mass function – galaxies: correlation function – Surveys

1 INTRODUCTION

The two most basic functions that characterize the observed galaxy population in the universe are the luminosity/stellar mass function (e.g. Cole et al. 2001; Bell et al. 2003; Baldry et al. 2008; Li & White 2009) and the spatial two-point correlation function (e.g. Jing et al. 1998; Norberg et al. 2001; Zehavi et al. 2005; Li et al. 2006b; Abbas & Sheth 2006; Zehavi et al. 2011). The former measures the number density of galaxies as a function of their luminosity or stellar mass, while the latter describes how strongly galaxies are clustered in space. In the current cold dark matter paradigm of structure formation (White & Rees 1978; Mo et al. 2010, and references therein), these two functions provide the key to understanding how galaxies form and evolve in the cosmic density field. Indeed, the observed luminosity/stellar mass function and correlation function have been

widely used to constrain theoretical models (e.g. Cole et al. 2000; Yang et al. 2003; Zheng et al. 2005; Lu et al. 2011; Artale et al. 2017; Springel et al. 2018; Wechsler & Tinker 2018).

The best way to obtain both the stellar mass function and correlation function is through the use of spectroscopic surveys of galaxies, where distances of individual galaxies can be estimated from spectroscopically-measured redshifts and stellar masses can be estimated from the spectra combined with multi-band photometry (Ilbert et al. 2006; Pozzetti et al. 2007; Boquien et al. 2019). A lot of efforts have been made to measure the two functions using various redshift surveys. For example, in the low- z universe, galaxy stellar mass function has been estimated from 2-degree Field Galaxy Redshift Survey (2dFGRS; Cole et al. 2001), Sloan Digital Sky Survey (SDSS; Li & White 2009) and Galaxy and Mass Assembly survey (GAMA; Baldry et al. 2012), while the two point correlation function has been measured from the Las Campanas Survey (e.g. Jing et al. 1998), 2dFGRS (e.g. Madgwick et al. 2003), SDSS (e.g. Li et al. 2006b;

* Contact e-mail: mengjc18@mails.tsinghua.edu.cn

† Contact e-mail: cli2015@tsinghua.edu.cn

Zehavi et al. 2011) and GAMA (e.g. Farrow et al. 2015). At higher redshift, galaxy stellar mass function has been measured from DEEP2 Galaxy Redshift Survey (DEEP2; Bundy et al. 2003), zCOSMOS (Pozzetti et al. 2010), VIMOS-VLT Deep Survey (VVDS; Pozzetti et al. 2007), and The VIMOS Public Extragalactic Redshift Survey (VIPERS; Davidzon et al. 2013), while the two-point correlation function has been estimated from DEEP2 (Coil et al. 2006), zCOSMOS (Meneux et al. 2009; de la Torre et al. 2011), VVDS (Pollo et al. 2006) and VIPERS (Mohammad et al. 2018).

To facilitate comparisons with model predictions, statistical measurements of the galaxy population, such as the stellar mass function and correlation function, are useful only when the samples used for the measurements are well defined. However, owing to observational limitations, real samples usually contain complex selection effects which make them incomplete in sampling the galaxy population we are interested in. Such incompleteness is particularly important for galaxies at high redshift (Ilbert et al. 2005; Pozzetti et al. 2010) where observational limitations are severer than galaxies in the low- z universe. High- z samples are usually not completely magnitude-limited, but selected using a combination of magnitude and color criteria (Lilly et al. 2009). In addition, the redshift sampling is also incomplete because of limits on spectroscopic targets, the limited number of fibers, fiber collisions in dense regions, and the lack of strong spectral lines of individual galaxies to estimate the redshift reliably. For example, the overall redshift sampling rate is only about 55% for the zCOSMOS-bright survey (Knobel et al. 2012) and about 50 – 70% for the forthcoming Prime Focus Spectrograph galaxy evolution survey (PFS, Takada et al. 2014), much lower than the sampling rate of nearly 100% for the low- z surveys such as SDSS (York et al. 2000). The sampling rates in general are not even uniform across the sky (de la Torre et al. 2011) and may depend on intrinsic properties of galaxies (Zucca et al. 2009). The observed samples are thus a biased sampling of the underlying galaxy population whose statistical properties are subjects of our interest. Clearly, the effects of such bias need to be corrected. In practice, almost all high- z spectroscopic surveys are based on deep photometric surveys with multi-waveband data (Laigle et al. 2016; Aihara et al. 2018) that can be used not only to obtain photometric redshift but also to estimate color, luminosity and stellar mass of individual galaxies (Muzzini et al. 2013; Laigle et al. 2016). This information can be combined with the spectroscopic data to provide a more faithful representation of the targeted galaxy population.

Another limitation on current high redshift galaxy surveys is that the samples are relatively small so that cosmic variance is a serious concern (Somerville et al. 2004; Driver & Robotham 2010; Moster et al. 2011). To quantify cosmic variance and the effects due to sample selection, the best way is to use realistic mock catalogs that follow the observational selection criteria closely. The goal of this paper is to develop methods that can be used to measure galaxy stellar mass function and correlation function from high-redshift surveys that are significantly incomplete in sampling. Our methods combine spectroscopic galaxies with those in the parent photometric survey to make full use of the information provided by the observational data. We calibrate and test our methods using detailed mock catalogs that mimic real observations with different selection criteria and com-

pleteness. These mock catalogs are also used to investigate cosmic variances expected from samples of different sizes. As applications, we apply our method to two surveys: the existing zCOSMOS-bright survey (Lilly et al. 2007, 2009) and the upcoming PFS galaxy evolution survey (Takada et al. 2014). In a parallel paper (Wang et al. 2020), we use the same mock catalogs to test a new group finding algorithm, developed specifically for identifying galaxy groups/clusters in high- z galaxy surveys.

The paper is organized as followed. In § 2 we describe the simulation and the galaxy formation model we use to construct the mock catalogs. In § 3 we describe our method for the constructions of the mock catalogs. In § 4, we describe the effects of the sample incompleteness in high- z survey on the measurements of galaxy luminosity/mass function and correlation function, as well as the methods to correct these effects. We then apply our mock catalogs and measuring methods to the zCOSMOS-bright survey in § 5 and the PFS galaxy survey in § 6, respectively. We summarize our results in § 7. Throughout the paper, we assume the WMAP5 cosmology (Dunkley et al. 2009; Komatsu et al. 2009) with the density parameter $\Omega_m = 0.258$ and the Hubble constant $h = 0.72$.

The mock catalogs for the zCOSMOS and PFS surveys constructed in this paper and our measurements of galaxy properties in the zCOSMOS-bright sample are available through https://github.com/mjc18/data_high-z_mock.

2 SIMULATION AND GALAXY MODEL

In this section, we first introduce the simulation and the galaxy formation model we use to construct mock catalogs, and then describe the methods we use to assign luminosities to model galaxies.

2.1 The Simulation

We use the ELUCID simulation carried out by Wang et al. (2016) to construct the mock catalogs. The ELUCID is a large N -body numerical simulation using 3072^3 dark matter particles in a cubic box of 500 Mpc/h on one side. The mass of a dark matter particle is $3.088 \times 10^8 M_\odot/h$. The simulation assumes the WMAP5 cosmology, which is a flat Λ CDM universe with a matter density parameter of $\Omega_m = 0.258$ and a Hubble constant given by $h \equiv H_0/(100 \text{ km/s/Mpc}) = 0.72$. The simulation was run from redshift $z = 100$ to $z = 0$, and 100 snapshots were output between $z = 18.4$ and $z = 0$. Dark matter halos and their substructures are identified with the friends-of-friends (FOF) and SUBFIND algorithms (Springel et al. 2005). A more detailed description of the simulation can be found in Wang et al. (2016).

2.2 The empirical model of galaxies

We populate the dark matter (sub-)halos in the ELUCID simulation with galaxies of different stellar masses and multi-band luminosities. To this end, we first assume that each sub-halo hosts a galaxy and we assign a stellar mass to the galaxy using the empirical model of galaxy formation developed in Lu et al. (2014, 2015). The detail of this process is described in Chen et al. (2019). In short, the model

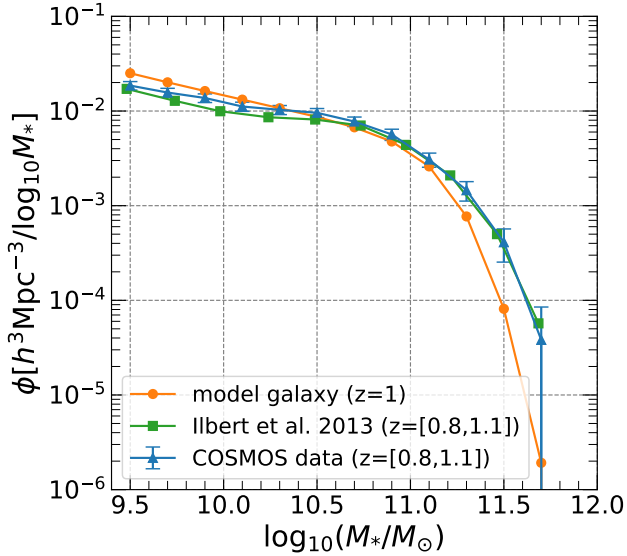


Figure 1. The stellar mass function at $z \sim 1$. The orange curve is for model galaxies in the simulation and the blue curve is the measurement obtained with the zCOSMOS-bright sample, which we used to calibrate the luminosity and color assignment for the model galaxies. The green curve is the measurement from Ilbert et al. (2013) based on an earlier sample of zCOSMOS.

assumes that galaxies form at the center of dark matter halos, and the growth of central galaxies is a function of dark matter halo mass and redshift. A central galaxy becomes a satellite if its host halo is accreted into a more massive halo and becomes a sub-halo. Thereafter the star formation rate of the galaxy (thus its growth) is suppressed due to some environmental quenching processes. The positions and velocities of galaxies are determined by those of their host halos (for centrals) or sub-halos (for satellites). The stellar mass is obtained by integrating the SFR along the branches of the halo merger tree. In what follows these galaxies are referred to as *model galaxies*.

Figure 1 displays the stellar mass function for the model galaxies in the simulation, plotted as solid circles connected by the orange line. For comparison, the stellar mass function estimated by Ilbert et al. (2013) from the COSMOS galaxy sample is plotted as solid squares connected by the green line. Note that this plot is not meant to make a quantitative comparison between our model prediction and observational data. Rather, the qualitative match between the two demonstrates that our model galaxy population provides a realistic sample to construct mock catalogs.

2.3 Luminosity Assignment for Model galaxies

We assign luminosities in different bands to each of the model galaxies. This is done in two steps. First we obtain the luminosity in a given band, represented by the corresponding rest-frame absolute magnitude (M_1), according to the relationship between the stellar mass and M_1 calibrated by observations (see below). Second, the luminosities in other bands are determined using the corresponding color indices, $M_1 - M_i$ ($i = 2, 3, \dots$), where M_i is the rest-frame absolute

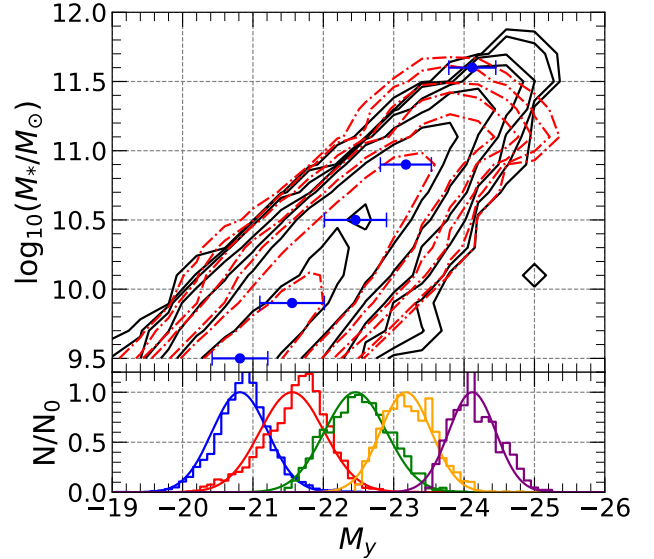


Figure 2. The upper panel shows the contours of the galaxy number density in the plane of stellar mass M_* versus y -band absolute magnitude M_y . The black lines are for the data from zCOSMOS2015 and the red dash lines are for model galaxies in our simulation. The lower panel shows the histogram of M_y in different intervals of $\log_{10} M_*$ and the lines are the best-fit Gaussians. The blue dots with error bars in the upper panel show the M_* - M_y relation and the Gaussian FWHM obtained from the fits in the lower panel.

magnitude in the i th band. In this step we also use the age of a sub-halo when determining the color of the galaxy it hosts, as detailed below.

We use the photometric data in the COSMOS2015 catalog (Laigle et al. 2016) to calibrate our model for the luminosities of model galaxies. The COSMOS field has been observed in 38 bands, covering a wide wavelength range from the ultraviolet to the far-infrared. The data thus enables precise estimates of both photometric redshifts (photo- z) and other galaxy properties, such as stellar mass and multi-band luminosities. We have estimated the galaxy stellar mass function using the COSMOS galaxy sample provided by Laigle et al. (2016). The result, plotted as the triangles connected by the blue line in Figure 1, is in good agreement with the stellar mass function published in Ilbert et al. (2013). We use the public software CIGALE (Boquien et al. 2019) to fit the spectral energy distribution (SED) of the COSMOS galaxies, and estimate the rest-frame absolute magnitude in a given band by convolving the best-fit rest-frame spectrum with the photometric response curve of the band. We adopt the photometric redshifts provided by Laigle et al. (2016) during the fitting.

We divide the galaxies in the COSMOS2015 catalog into successive bins of stellar mass M_* , each with a fixed width of 0.2 dex. For each M_* bin, we fit the distribution of M_1 (absolute magnitude of the chosen band) with a Gaussian function. For a model galaxy falling in the same M_* bin, we randomly assign an absolute magnitude according to the Gaussian fit. Figure 2 shows the distribution of the COSMOS2015 galaxies in the $\log_{10} M_* - M_y$ plane, where M_y

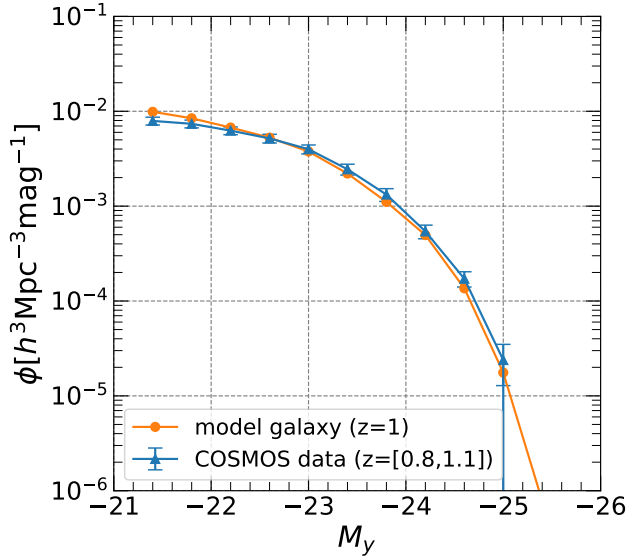


Figure 3. The y -band luminosity function of galaxies at $z \sim 1$. The orange curve is for the model galaxies in the simulation and the blue curve is estimated from the zCOSMOS2015 data which we use to calibrate our method to assign the luminosity and colors for our model galaxies.

is the y -band absolute magnitude. The black contours are based on the observational data, while the red dashed contours are based on the assigned M_y . The lower panel shows the M_y distributions and the corresponding Gaussian fits in different mass bins. As can be seen, the assigned absolute magnitudes reproduce the mass-luminosity relation very well, in terms of both the average relation and the scatter. Figure 3 compares the y -band luminosity functions at $z \sim 1$ estimated from the COSMOS2015 sample using the real data (blue triangles) and the assigned absolute magnitudes (orange circles). Again the two functions agree with each other very well.

We assign absolute magnitudes in bands other than M_1 by applying the sub-halo age distribution matching method (Hearin & Watson 2013). The method assumes that, at fixed stellar mass, the color of a galaxy is a monotonous function of the age of its host halo, usually quantified by z_{starve} , the redshift at which the host halo started to be starved of cold gas supply. In general, z_{starve} is expected to be related to the halo mass assembly history. The following three definitions have been adopted for the same purpose (e.g. Wechsler et al. 2002; Behroozi et al. 2013; Hearin & Watson 2013):

- (i) z_{char} , the highest redshift at which the halo mass exceeds $10^{12} M_{\odot}/h$;
- (ii) z_{acc} : the redshift at which a halo becomes a subhalo and remains such thereafter;
- (iii) z_{form} : the redshift after which the mass accretion by the halo is negligible.

Following common practice, we define z_{starve} as the maximum of the three redshifts defined above,

$$z_{\text{starve}} = \text{Max}\{z_{\text{char}}, z_{\text{acc}}, z_{\text{form}}\}. \quad (1)$$

It is known that galaxies of given mass or luminosity can be divided into two populations in the color space. In each

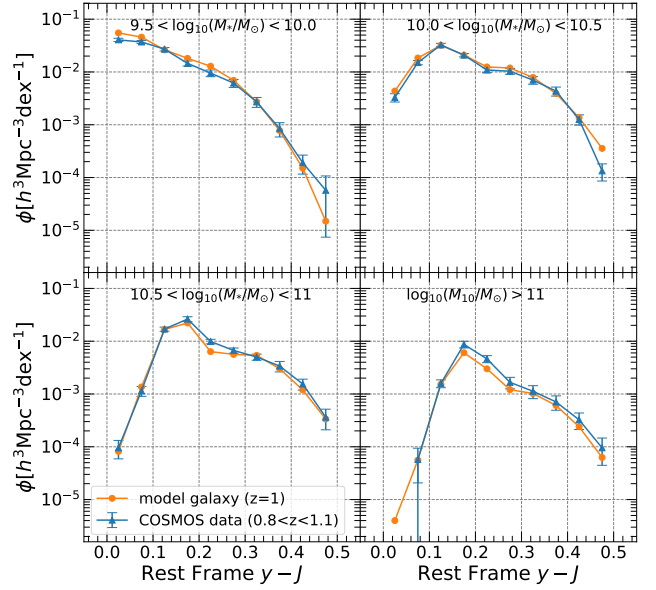


Figure 4. The distribution of the rest-frame $y - J$ color for model galaxies (orange curves) and obtained from the zCOSMOS2015 data (blue curves with error bars).

stellar mass interval, we fit the distribution of the color index $M_1 - M_i$ of the COSMOS2015 galaxies by a bi-Gaussian function, so as to obtain a mass-dependent color distribution function, $n(M_1 - M_i | M_*)$. Similarly, for model galaxies, we obtain the mass-dependent distribution function of z_{starve} , $n(z_{\text{starve}} | M_*)$. For each model galaxy, we then assign a $M_1 - M_i$ color by matching the number density of the observed galaxies above a given color threshold to that of the model galaxies above a certain threshold in z_{starve} :

$$n_{\text{mod}}(> z_{\text{starve}} | M_*) = n_{\text{obs}}(> (M_1 - M_i) | M_*). \quad (2)$$

By solving this equation we obtain a monotonic relation between z_{starve} and $(M_1 - M_i)$, which enables us to assign an $(M_1 - M_i)$ color (thus M_i for the known M_1) to each model galaxy according to its z_{starve} . Figure 4 compares the distributions of the $(y - J)$ color of model galaxies in different stellar mass bins (orange curves) to the corresponding distributions obtained from COSMOS2015 (blue curves). The two agree with each other very well, demonstrating that the properties of the galaxy population are well represented by our model galaxies.

3 METHODOLOGY OF CONSTRUCTING MOCK CATALOGS

In this section we describe our method for constructing mock catalogs. Specifically, we will construct mock catalogs based on the selection criteria of two spectroscopic surveys of high- z galaxies: the existing zCOSMOS survey and the upcoming Subaru/PFS galaxy evolution survey. We would like to emphasize, however, that our method is by no means limited to the two surveys; the basic methodology should be equally applicable to any surveys with incompleteness produced by color selection and spectroscopic sampling.

3.1 The zCOSMOS Survey and the PFS galaxy evolution survey

The zCOSMOS is a large redshift survey of galaxies in the COSMOS field, carried out with the VIMOS spectrograph on the 8-meter ESO Very Large Telescope (e.g. Lilly et al. 2007). The survey consists of two components. The first is zCOSMOS-bright, a magnitude-limited sample of about 20,000 galaxies with $I_{AB} < 22.5$ and $0.1 \lesssim z \lesssim 1.2$ that covers the whole 1.7 deg^2 COSMOS field. The another is zCOSMOS-deep, a sample consisting of about 10,000 galaxies with $1.5 \lesssim z \lesssim 3$ selected through color-selection criteria in the central $\sim 1 \text{ deg}^2$ of the COSMOS field. Both samples are targeted to have a sampling rate of $\sim 70\%$, but the actual sampling rate is 56% for zCOSMOS-bright (Knobel et al. 2012) and 55% for zCOSMOS-deep (Diener et al. 2013). For our analysis, we only use the zCOSMOS-bright Sample.

The Prime Focus Spectrograph (PFS) project (Takada et al. 2014) is one of the next-generation multi-object spectroscopic surveys to be accomplished on the Subaru 8.2-meter telescope. The PFS is a massively multiplexed, optical and near-infrared (NIR) fiber-fed spectrometer, equipped with 2394 re-configurable fibers distributed in a wide hexagonal field of view with a diameter of 1.3 degrees. The PFS project will conduct three major survey programs, dedicated to fundamental and important questions in cosmology, galaxy evolution and the origin of the Milky Way, respectively. In this paper we consider only the galaxy evolution survey, and we will refer it as the ‘PFS survey’ or ‘PFS galaxy survey’ for simplicity, unless otherwise stated. The PFS galaxy survey aims to obtain spectroscopy for $\sim 256,000$ galaxies in the redshift range $0.7 < z < 1.7$, distributed over three separated fields (E-COSMOS, XMM-LSS and DEEP2-3) that have deep imaging in both optical and NIR. The total sky area of these fields is $\sim 14.5 \text{ deg}^2$, and will be covered by 13 PFS pointings. Targets of the galaxy sample are selected to fall in the anticipated redshift range, $0.7 < z < 1.7$, using photometric redshifts estimated from the available imaging data, and are limited by the y -band apparent magnitude as $y < 22.5$. At $z > 1$, targets fainter than $y = 22.5$ may also be included if their J -band magnitude $J < 22.8$. The redshift sampling rate is about 50% for the sample at $z < 1$ and 70% for that at $z > 1$.

3.2 Constructing light-cones

We construct mock catalogs for a given survey (zCOSMOS-bright or the PFS in our case) following the commonly-used two-step method detailed in Blaizot et al. (2005). First, an observing lightcone covering the same volume and redshift range as the real survey is constructed using simulation snapshots in the same redshift range as the survey. Next, model galaxies are selected in the lightcone to form a mock catalog, and their apparent properties, such as apparent magnitudes in different bands, are computed taking into account the selection effects of the real survey.

Due to its limited box size, the simulation box of a given snapshot has to be stacked to achieve a sufficiently large volume, taking advantage of the periodic boundary condition. However, because of the periodic boundary condition the same structure can appear repeatedly if observed along a coordinate axis of the simulation box. Following Blaizot et al.

(2005), we apply the technique of random tiling to overcome this problem. For each simulation box, we apply the following transformations successively: (i) a random translation along each of the three axes; (ii) rotations of $0, \pi/2, \pi, 3\pi/2$ around each axis; (iii) the inversion of one randomly chosen axis. In principle, these transformations combined can prevent the presence of replicated structure along the line of sight. By applying this random tiling scheme many times, we can generate a set of different mock catalogs, in which the same (simulated) universe is virtually observed from different directions.

The stacked and randomly transformed snapshots of different redshifts are then used to construct the lightcone. We fill in successive intervals of comoving distance with the corresponding snapshots. Specifically, for an interval of comoving distance,

$$\frac{D_i + D_{i-1}}{2} < D < \frac{D_i + D_{i+1}}{2}, \quad (3)$$

we use model galaxies from the snapshots at redshift z_i . For each model galaxy, we calculate a cosmological redshift z_{cos} from its comoving distance. The peculiar velocity along the line of sight, v_{pec} , which is estimated using the velocity of the (sub-)halo which the galaxy live in, is added to the z_{cos} to give a spectroscopic redshift z_{spec} :

$$z_{\text{spec}} = \sqrt{\frac{1 + v_{\text{pec}}/c}{1 - v_{\text{pec}}/c}}(1 + z_{\text{cos}}) - 1. \quad (4)$$

We also estimate a photometric redshift (photo- z) for each galaxy by including the typical uncertainty of photo- z of the survey. Assuming the photo- z error in $\frac{\Delta z}{1+z}$ to be σ , we have

$$z_{\text{photo}} = z_{\text{spec}} + (1 + z_{\text{spec}}) \times N(0, \sigma^2), \quad (5)$$

where $N(0, \sigma^2)$ is the normal distribution with the mean equal to zero and with the standard deviation equal to σ .

Finally, we finish the construction of the lightcone by excluding model galaxies outside the sky coverage of the survey. As mentioned above, by applying the random tiling many times, we can generate a set of different lightcones to form a set of mock catalogs. As an example, Figure 5 shows one of the lightcones made for the DEEP2-3 field of the PFS galaxy survey, projected onto the RA and redshift plane. The red and blue dots represent galaxies with red and blue colors according to $(y - J)$, respectively.

3.3 Incorporating observational selection effects

We calculate apparent magnitudes of model galaxies in a given lightcone according to their absolute magnitudes and redshifts, and we construct a mock catalog by applying the same selection effects as the real survey. The apparent magnitude of the i -th band is given by

$$m_i = M_i + 5 \log_{10}(D_L) + 25 + K \cdot \log_{10}(1 + z), \quad (6)$$

where M_i is the absolute magnitude of the i -th band, D_L is the luminosity distance in units of Mpc, and K is the k -correction. The value of K is not available from our model. We estimate the value of K using the COSMOS2015 galaxy catalog, assuming that the galaxies of the same luminosities and colors have a similar spectral energy distribution. For a

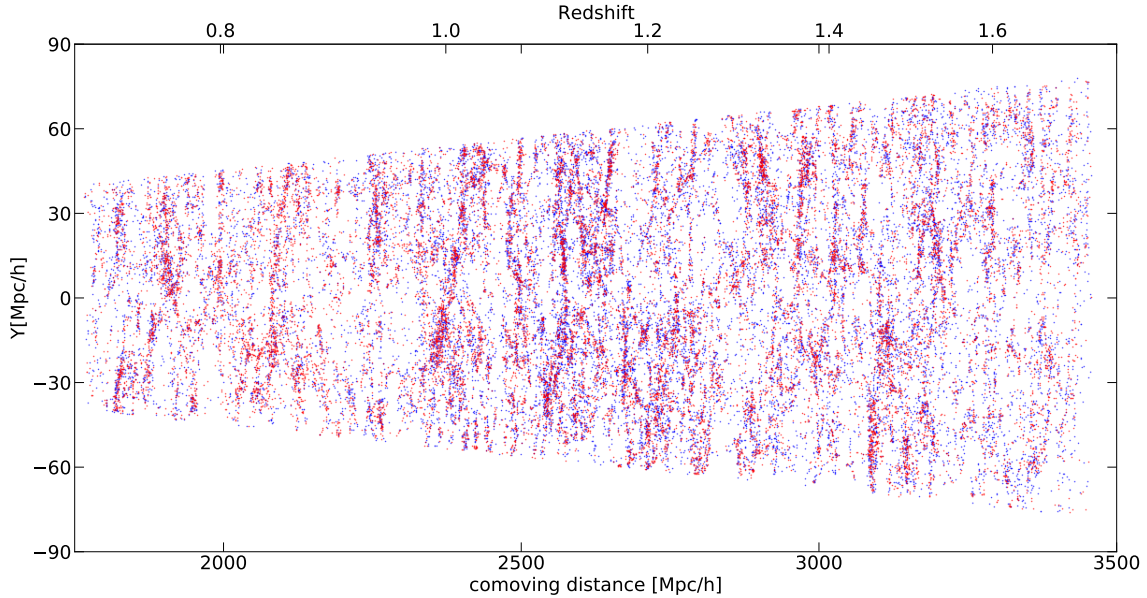


Figure 5. The lightcone of the PFS survey in DEEP2-3 field. The range of the declination is $-0.3^\circ \leq \delta \leq 0.3^\circ$. The color of a point represents the intrinsic ($y - J$) color of the galaxy.

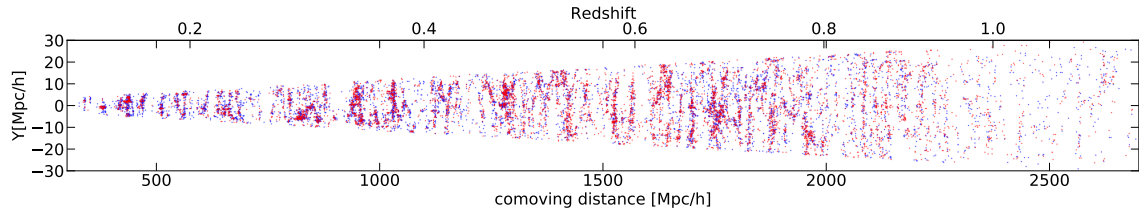


Figure 6. The lightcone of the zCOSMOS survey. The range of the declination is $1.94^\circ \leq \delta \leq 2.54^\circ$. The color of a point represents the intrinsic ($B - I$) of the galaxy.

given model galaxy, we identify a real galaxy from the COSMOS2015 catalog by matching the absolute magnitude, M_1 , and the color index $M_1 - M_i$, where the bands for M_1 and M_i may be different for different surveys (e.g. M_y and M_J for the PFS galaxy survey). The K value of the real galaxy, which was estimated from the best-fit rest-frame spectrum of the galaxy by spectral fitting (see § 2.3), is then assigned to the model galaxy.

The details of the target selection strategy may vary from survey to survey, but in general the targets are selected to form a magnitude-limited sample according to the apparent magnitude in a specific band. For instance, the SDSS main sample targeted galaxies with r -band magnitude $r \lesssim 17.77$ (York et al. 2000). For high- z surveys, additional redshift criteria, based on color-color diagrams or photometric redshifts, are used to exclude targets outside the aimed redshift range. The zCOSMOS-bright sample selected galaxies with $I_{AB} < 22.5$ and $0.1 < z \lesssim 1.2$, and the PFS galaxy survey will observe galaxies with $0.7 < z < 1.7$ and $y < 22.5$ (if at $0.7 < z < 1.7$) or $J < 22.8$ (if at $z > 1$).

In most spectroscopic surveys, especially those at high redshift, only a fraction of the targets satisfying the redshift and magnitude limits can be included in the spectroscopic sample, due to the limited number of fibers, finite observing time, imperfect redshift identification and a variety of other

limitations (e.g. obscuration by bright stars, bad weather, fiber collisions). In general, these effects combined can be quantified by a sampling rate, defined as the fraction of the targets that are actually observed and included in the final sample. The sampling rate may vary across the survey coverage as well. This is indeed the case for the zCOSMOS survey, where the angular sampling is inhomogeneous, but a function of the right ascension (RA) and redshift, as described in Lilly et al. (2007) and Lilly et al. (2009). The RA-dependence of the sampling rate due to incomplete targeting was presented in figure 5 of de la Torre et al. (2011), while the redshift-dependent sampling rate due to imperfect redshift identification (redshift success rate) was shown in figure 9 of Lilly et al. (2007). We apply the RA and redshift-dependent sampling rate to the zCOSMOS lightcones, in addition to the redshift and magnitude cuts as described above. This gives rise to a set of mock catalogs for the zCOSMOS-bright survey, with an average sampling rate of $\sim 48\%$ for the whole area and $\sim 56\%$ for the central region, well consistent with the sampling rate of the real sample (Knobel et al. 2012).

For the PFS galaxy survey, the angular sampling is expected to vary across the survey area as well. The inhomogeneity is mainly caused by the fact that the spectroscopic target sampling becomes increasingly low in the sky where the target density is high, because two fibers cannot be posi-

tioned too closely. The fiber assignment strategy of the PFS survey is described in Sunayama et al. (2019) and Shimono et al. (2016), and a software named Exposure Targeting Software (ETS)¹ is designed to implement the assignment for a given sample of targets. We apply this software to our mock catalogs, by requiring an average sampling rate of 50% for $0.7 < z < 1$ and 70% for $1 < z < 1.7$, as planned for the upcoming PFS galaxy survey.

4 EFFECTS OF SAMPLE INCOMPLETENESS AND THEIR CORRECTIONS

In this section we describe our methodology of measuring the number density and clustering of galaxies from high- z surveys. We will measure three statistical quantities: the luminosity function of galaxies (LF), $\Phi(M)$, galaxy stellar mass function (GSMF), $\Phi(M_*)$, and the projected two-point correlation function (2PCF), $w_p(r_p)$. Sample incompleteness due to observational selection effects described in § 3.3 can cause biases in the measurements, if not properly corrected. We therefore will also discuss potential biases that may be caused by the sample incompleteness and develop methods to correct them. These methods will be applied to the zCOSMOS and PFS galaxy samples in the next two sections, respectively.

4.1 Methodology to Measure LF, GSMF and 2PCF

4.1.1 Luminosity Function and Stellar Mass Function

The luminosity function and stellar mass function are usually estimated using two different methods: the V_{\max} -weighting method (Schmidt 1968) and the maximum likelihood method (STY, Sandage et al. 1979). We use the V_{\max} -weighting method. For the i -th galaxy with an absolute magnitude $M_{1,i}$, we determine a maximum redshift, $z_{\max,i}$, at which $M_{1,i}$ corresponds to the limiting apparent magnitude that was used to select the sample. Given the survey area, $z_{\max,i}$ defines a maximum volume, $V_{\max,i}$, over which galaxy targets with the same absolute magnitude, $M_{1,i}$, can be observed in the apparent magnitude-limited sample. The inverse ratio of this volume to the total survey volume (given by the upper boundary of the redshift of the survey), $V_{\text{survey}}/V_{\max,i}$, is used to weight the galaxy and to statistically correct for the luminosity-dependent incompleteness of the survey volume. As we will show below, in addition to the $1/V_{\max}$ weighting, additional weights are needed to account for other sources of incompleteness.

Due to the limited depth of a survey, both the luminosity and stellar mass functions can only be measured down to a limited luminosity or mass. The limit for the luminosity function measured for galaxies at a given redshift can be determined by the apparent magnitude limit of the survey. For the stellar mass function, however, the determination of the stellar mass limit $M_{*,\min}(z)$ is not straightforward. If the survey uses the apparent magnitude of the j th-band to select the targets, we use the symbol m_j to represent the apparent magnitude of the galaxy in this band and $m_{j,\text{lim}}$ to

denote the magnitude limit of the survey. Following Pozzetti et al. (2010), we first estimate a mass limit, $M_{*,\text{lim}}$, for each galaxy using

$$\log_{10}(M_{*,\text{lim}}) = \log_{10}(M_*) + 0.4(m_j - m_{j,\text{lim}}) \quad (7)$$

The galaxies are divided into successive redshift bins with a fixed width of $\Delta z = 0.2$. For each redshift bin we select the 20% faintest galaxies according to the j -th band apparent magnitude, and obtain the distribution of their $M_{*,\text{lim}}$. The minimum stellar mass at a given redshift, $M_{*,\min}(z)$, is then defined by the upper envelope of the distribution, which is the value of $M_{*,\text{lim}}$ that encloses 95% of the galaxies in the distribution. We will come back to this later when we apply the method to specific surveys.

4.1.2 Projected Two-point Correlation Function

We use the Landy-Szalay estimator (Landy & Szalay 1993) to estimate the correlation function. For a given galaxy sample \mathcal{D} (either a mock galaxy sample or a sample of real galaxies) and the corresponding random sample \mathcal{R} that is constructed to have the same selection effects as sample \mathcal{D} (see below), we first estimate the redshift-space correlation function as:

$$\xi(r_p, \pi) = \frac{1}{RR} \times \left[\frac{N_r(N_r - 1)}{N_d(N_d - 1)} DD - 2 \frac{N_r}{N_d} DR + RR \right], \quad (8)$$

which is a function of the pair separations both perpendicular (r_p) and parallel (π) to the line of sight. Here, N_d and N_r are the sample sizes of \mathcal{D} and \mathcal{R} , respectively, and DD , RR and DR are the counts of galaxy-galaxy pairs in the galaxy sample, random-random pairs in the random sample, and galaxy-random cross pairs between the two samples, respectively. The pair counts are also functions of r_p and π . Note that, when estimating N_d and pair counts involving sample \mathcal{D} , the galaxies in \mathcal{D} are usually weighted to take into account the effect of sample incompleteness that are not perfectly included in the random sample (see below for details).

To reduce effects of redshift distortions, we use the projected 2PCF, defined by integrating $\xi(r_p, \pi)$ along the line of sight:

$$w_p(r_p) = 2 \int_0^{+\infty} \xi(r_p, \pi) d\pi = 2 \sum_{i=1}^n \xi(r_p, \pi_i) \Delta\pi_i. \quad (9)$$

We choose $n = 40$ and $\Delta\pi_i = 1 \text{Mpc/h}$, so that the summation runs from $\pi_1 = 0.5 \text{Mpc/h}$ up to $\pi_{40} = 39.5 \text{Mpc/h}$ with a constant interval of 1Mpc/h .

By construction, the random sample is required to contain the same selection effects as the galaxy sample. For a galaxy sample selected by the j th-band apparent magnitude with a magnitude limit of $m_{j,\text{lim}}$, we first create a spatial volume that is sufficiently large to contain the survey volume, and generate ‘‘random galaxies’’ by randomly distributing points within the survey boundary, in terms of both sky area and redshift range. Then, we estimate the j th-band luminosity function in different redshift intervals using the galaxy sample, and use the luminosity function to assign to each random galaxy an j th-band absolute magnitude M_j . Next, we assign a stellar mass M_* to each random galaxy according to the $M_* - M_j$ relation from the galaxy sample. For a given redshift interval, we divide galaxies in both the galaxy sample and the random sample into successive bins of M_j , each

¹ https://github.com/Subaru-PFS/ets_fiberalloc.

with a fixed width of 0.2 dex, and fit the distribution of M_* with a Gaussian for each M_j bin. For a random galaxy with a luminosity of M_j , a stellar mass is then randomly generated to statistically follow the Gaussian distribution in the corresponding M_j bin. Finally, for each random galaxy we calculate an j th-band apparent magnitude m_j according to its redshift, M_j , and k -correction. The value of k -correction is randomly selected from the galaxies in the galaxy sample with similar luminosity ($\Delta M_j < 0.2$ dex). We select random galaxies with $m_j < m_{j,\text{lim}}$ to form the final random sample.

4.2 Effects of Incompleteness in High- z Samples

In addition to the luminosity-dependent incompleteness that is straightforward to correct either with the $1/V_{\text{max}}$ weighting method or using random samples, as described above, there are three more incompleteness effects that have to be carefully taken into account. The first is that only a fraction of galaxy targets selected from the parent photometric sample with the redshift and magnitude limits can be included in the final spectroscopic sample. We refer the effect arising from such incompleteness as *sampling rate effect*. The second is the *fiber collision effect* (or *slit collision effect* in slit mask spectroscopy), which prevents a close pair of galaxies from being observed simultaneously, and so can bias measurements of clustering on small scales. The last effect is caused by the flux selection criteria of the galaxy sample, which may bias against low-mass red galaxies because of their low flux in the observing band. Since the clustering of galaxies depends on their color, this bias may affect measurements of galaxy clustering. This effect is referred to as the *flux limit effect*.

The sampling rate effect is contributed by two factors. The first is the incomplete sampling of galaxy targets selected for observations, which may vary from region to region due to constraints on the arrangement of slits or fibers. The sampling rate caused by this effect usually depends only on the position and the local distribution of galaxies in the sky, independent of the properties of the target galaxies, as shown in [Figure A1](#) for the case of the PFS galaxy survey. Another source of the sampling rate effect is the imperfect redshift determination of a target galaxy because the spectrum obtained is too poor. The success rate of redshift determination depends on galaxy properties and redshift: one expects higher success rates for brighter emission-line galaxies at lower redshifts than for fainter galaxies with weak emission lines at higher z . We define the target sampling rate as $f_s(\text{RA}, \text{Dec})$, and the redshift success rate as $f_z(z, \theta_k)$, where (RA, Dec) is the sky position of the galaxy, z is the redshift and θ_k is a set of properties of the galaxy (e.g. luminosity, color, galaxy type, etc). The combined effect is then given by the product of the two rates.

The effect of fiber (or slit) collisions is caused by the constraints of the instrument, such as the slit mask design for zCOSMOS survey ([Bottini et al. 2005](#)) and the fiber assignment strategy for PFS survey ([Sunayama et al. 2019](#)). The effect may vary from survey to survey quantitatively, but a generic consequence of this effect is that a pair of galaxies too close to each other in angular position cannot each be assigned a fiber (or slit) at the same time. This will lead to an underestimate of the clustering power on scales smaller than the minimum separation allowed for two

neighbouring fibers. For instance, this scale is about $30''$ for the PFS, corresponding to 0.260-0.497 Mpc/h for $0.7 < z < 1.7$.

The flux limit effect may also cause an underestimated measurement of the small-scale galaxy clustering, and the effect is more significant for red galaxies compared to blue galaxies of similar masses. The reason is that, at fixed mass, red galaxies in general have larger mass-to-light ratios than blue galaxies. Thus, for a sample of galaxies in a given stellar mass range, red galaxies have a higher probability to be excluded by the flux limit owing to their higher mass-to-light ratios. Since red galaxies tend to be more strongly clustered than blue galaxies at fixed mass, the correlation function obtained from a flux-limited sample will be an underestimate of the correlation function of a truly mass-limited sample. This effect is expected to be more important at higher z and when the observational band used for target selection corresponds to a bluer rest-frame band.

4.3 Methods to correct effects of incompleteness

In this subsection, we will describe the methods for correcting the effects of incomplete sampling, fiber collision and flux limit. The goal is to obtain unbiased measurements of the LF, GSMF and projected 2PCF from incomplete redshift samples.

4.3.1 Weighting Scheme for Correcting the Sampling Rate Effect

To correct the sampling rate effect, we have to accurately estimate both the sky position-dependent sampling rate, $f_s(\text{RA}, \text{Dec})$, and the redshift success rate, $f_z(z, \theta_k)$. We estimate $f_s(\text{RA}, \text{Dec})$ using the Voronoi tessellation. This algorithm divides the whole survey area into non-overlapping polygons, so that each polygon contains one (and only one) observed galaxy and that every position within the survey area is covered by one (and only one) polygon. The sampling rate of the J -th polygon is estimated by the inverse of the total number of targets in the parent photometric sample: $f_{s,J} = 1/N_{p,J}$. Thus, the sampling rate is a constant within a given polygon, and each galaxy in the observed sample is assigned the sampling rate of the polygon in which it resides: $f_{s,i} = f_{s,J}$, where i refers to the i -th galaxy and J to the J -th polygon.

Redshift success rate for each galaxy in the spectroscopic sample, $f_z(z, \theta_k)$, is a function of redshift, z , and a set of properties of the galaxy, θ_k . In principle, one could consider n properties, and estimate the success rate function, $f_z(z, \theta_k)$, in the $(n + 1)$ -dimensional parameter space using the ratio between the number of successfully-measured redshifts, N_{succ} , and the number of spectroscopic targets, N_{obs} . One can then estimate $f_{z,i}$ for each galaxy in the galaxy sample.

Once $f_{s,i}$ and $f_{z,i}$ are obtained for the i -th galaxy, we assign to it a weight defined as

$$w_{\text{sky},i} = \frac{1}{f_{s,i} f_{z,i}}. \quad (10)$$

This weight will be used to correct for the sampling rate effect of the survey when we estimate both the number density and clustering of the galaxies. For the measurements of

LF and GSMF with the V_{\max} -weighting method, we multiply the V_{\max} weighting, $V_{\text{survey}}/V_{\max,i}$, by the sky position-dependent weight $w_{\text{sky},i}$ given by Equation 10 to give the total weight for a given galaxy:

$$w_{\text{tot},i} = \frac{V_{\text{survey}}}{V_{\max}} \times w_{\text{sky},i} = \frac{V_{\text{survey}}}{V_{\max}} \times \frac{1}{f_{s,i} f_{z,i}}. \quad (11)$$

For the measurements of the projected 2PCF, we weight each galaxy in the galaxy sample by $w_{\text{sky},i}$ given by Equation 10 when computing DD , DR and N_d .

As we will show below using tests on mock samples of both zCOSMOS and PFS, the LF and GSMF can be fully reproduced with the weighting scheme described above, but one has to correct for the other two effects in order to measure the projected 2PCF accurately.

4.3.2 The Correction of Fiber Collision Effect

Following Hawkins et al. (2003) and Li et al. (2006b), we use the angular correlation function of the parent photometric sample to correct the fiber collision effect on the projected correlation function obtained from the spectroscopic sample. We first estimate the angular correlation for both the parent photometric sample ($w_p(\theta)$) and the spectroscopic sample ($w_s(\theta)$). Note that w_s is corrected for the Sampling Rate Effect described above. When computing the galaxy-galaxy pair count DD in Equation 8, we weight each pair by

$$F(\theta) = \frac{1 + w_p(\theta)}{1 + w_s(\theta)}, \quad (12)$$

where θ is the angular separation of the galaxy pair. As demonstrated in Li et al. (2006c), this weighting method works well in correcting the underestimation of the clustering on scales where fiber collision effect is significant.

4.3.3 The Correction of Flux limit Effect

We correct the bias caused by the flux limit effect with the help of two photometric samples: one is the parent photometric sample that includes all galaxies in the same redshift and mass ranges as the redshift survey sample (**sample p**), and the other is the subset of galaxies in this sample that meet the flux criteria of the survey sample (**sample p'**). For instance, for a given stellar mass range and a redshift interval $z_l < z < z_u$, **sample p** consists of all the galaxies from the parent photometric sample that fall in the same mass range and have photometric redshifts in the range of $z_l - 2\delta z < z_{\text{phot}} < z_u + 2\delta z$, where δz is the uncertainty of the photometric redshift, z_{photo} . We assume that the photometric redshift and stellar mass for galaxies in the photometric parent sample can be estimated from fitting the multi-band SED, e.g. by using data from the HSC imaging survey for the PFS targets. The range of photometric redshift is chosen so as to include most (if not all) of the correlated pairs in the sample, and simultaneously to minimize the computing time by removing uncorrelated pairs in the foreground and background. For PFS targets, $\delta z/(1+z) = 0.02 - 0.03$. For the redshift interval of $1.4 < z < 1.7$, for example, the photo- z range is set to $1.1 < z_{\text{phot}} < 2$. Since **sample p'** is a subset of **sample p**, the spectroscopic sample from the mock survey (**sample s**) is a subset of **sample p'** limited by the incomplete sampling and imperfect redshift determination.

Sample s and **sample p'** are essentially equivalent in terms of clustering. The problem is, however, that both **sample s** and **sample p'** are a biased subset of **sample p** due to the flux selection criteria, and that **sample p** is the complete and representative sample for the clustering of the galaxy population we want to measure. Unfortunately, it is hard to estimate $w_{\text{pp}}(r_p)$ accurately from the photometric sample owing to the large uncertainties in photo- z . Here we propose to estimate $w_{\text{pp}}(r_p)$ through the following relations:

$$b_s(r_p) = \frac{w_{\text{ss}}(r_p)}{w_{\text{sp}}(r_p)} = \frac{w_{\text{sp}'}(r_p)}{w_{\text{sp}}(r_p)} = \frac{w_{\text{pp}'}(r_p)}{w_{\text{pp}}(r_p)}, \quad (13)$$

where b_s is the relative bias of **sample s** (and equivalently **sample p'**) with respect to **sample p**, and $w_{\text{sp}'}$, w_{sp} and $w_{\text{pp}'}$ are cross-correlation functions between the two samples indicated by the subscripts. On the other hand, the factor b_s can also be defined by the ratio of the auto-correlation between **sample s** and **sample p**: $b_s = \sqrt{w_{\text{ss}}/w_{\text{pp}}}$. Thus, the auto-correlation of **sample p**, i.e. the corrected $w_p(r_p)$ of **sample s**, can be estimated as

$$w_{\text{ss,true}}(r_p) = w_{\text{pp}}(r_p) = \frac{w_{\text{ss}}(r_p)}{b_s^2(r_p)} = \frac{w_{\text{sp}}^2(r_p)}{w_{\text{sp}'}(r_p)}, \quad (14)$$

where the cross-correlation functions, $w_{\text{sp}'}$ and w_{sp} , can be estimated from the two photometric samples, **sample p** and **sample p'**, using the method described in Appendix B. In practice, for galaxies in **sample s**, we count the neighbours from **sample p** and **sample p'** as a function of r_p . These galaxy counts are then normalized by the expected mean counts to determine $w_{\text{sp}}(r_p)$ and $w_{\text{sp}'}(r_p)$, respectively. Finally, we obtain $w_{\text{ss,true}}$ using Equation 14, which is the unbiased projected 2PCF corrected for the flux limit effect.

5 NUMBER DENSITY AND CLUSTERING OF GALAXIES IN zCOSMOS

In this section we use the zCOSMOS-bright sample to measure the number density and clustering of galaxies, as quantified respectively by galaxy luminosity function (LF) and stellar mass functions (GSMF), as well as the projected two-point correlation functions (2PCF). We use the mock catalogs constructed in § 3 to test our methods described in § 4.3 before applying them to the real sample. The mock catalogs are also used to estimate the errors of the measurements in both GSMF and 2PCF. We note that the same statistics have been estimated for the zCOSMOS in previous studies (Zucca et al. 2009; Meneux et al. 2009; Pozzetti et al. 2010; de la Torre et al. 2011). The purpose of our analysis here is two-fold. First, we intend to improve the earlier measurements using information gathered from our mock catalogs. Specifically, we apply our weighting scheme to accurately account for the sky position-dependent sampling rate and to correct for biases caused by target selection, and we quantify errors caused by cosmic variance and statistical uncertainties. Second, we compare the measurements for the zCOSMOS sample with those for the PFS mock catalogs to predict the improvement in the measurements expected from the upcoming PFS survey.

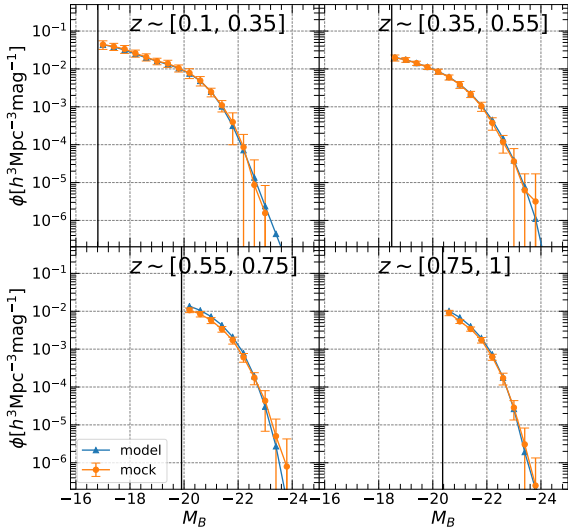


Figure 7. The B -band luminosity function as estimated from the mock catalog of the zCOSMOS-bright survey for four different redshift intervals (as indicated in each panel) is plotted as orange dots, and is compared to the *true* luminosity function of the model galaxies in the simulation plotted as the blue triangles. The black line in each panel indicates the lower limit of M_B to which the luminosity function can be measured. See the text for details.

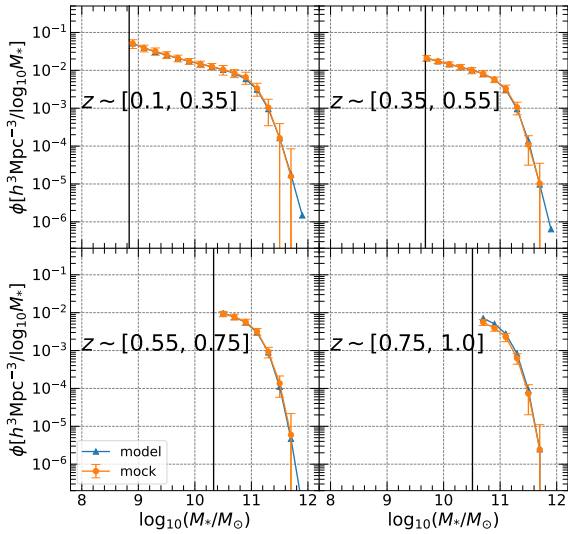


Figure 8. The stellar mass function estimated for four different intervals using the mock catalogs of the zCOSMOS-bright sample is plotted as the orange line, and is compared to the true mass function of model galaxies estimated from the simulation (the blue lines). The black line in each panel indicates the lower limit of M_* to which the mass function can be measured. See the text for details.

5.1 Galaxy Luminosity and Stellar Mass Functions in mock catalogs

We use the V_{\max} -weighting method described in § 4.1.1 to estimate the luminosity and stellar mass functions of galaxies in the zCOSMOS mock catalogs. The sample rate effect is corrected using the weighting scheme described in § 4.3.1. The sky position-dependent sampling rate $f_s(\text{RA}, \text{Dec})$ is

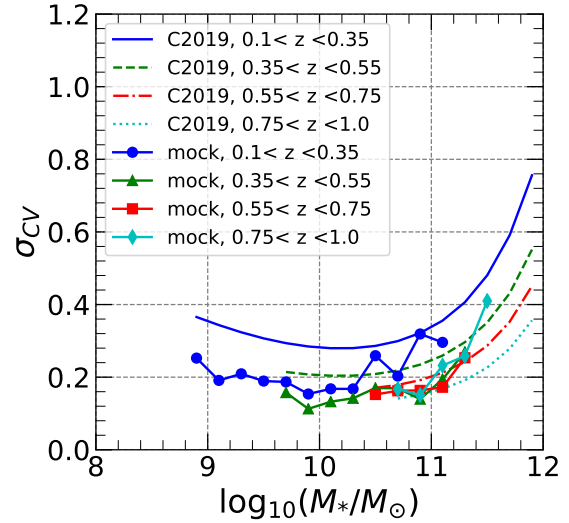


Figure 9. The fractional variance caused by cosmic variance of the stellar mass function estimated using mock catalogs for the zCOSMOS-bright survey, plotted as symbols connected by lines. Different colors are for different redshift intervals, as indicated. The lines of different styles/colors are predicted with the formula from Chen et al. (2019) (indicated as C2019).

estimated using the algorithm of Voronoi Tesselation. The success rate function is estimated in the redshift-color space, $f_z(z, U - V)$, as a function of the redshift in bins of $\Delta z = 0.2$ and the intrinsic $(U - V)$ color index, following Zucca et al. (2009). Each galaxy in a mock catalog is then weighted by the total weight given by Equation 11 when measuring the LF and GSMF. The limits of the luminosity function and galaxy stellar mass function are estimated with the method described in § 4.1.1.

Figure 7 displays the B -band luminosity functions estimated from the mock catalogs, for galaxies in four different redshift intervals as indicated. Figure 8 displays the measurements of GSMF for the same redshift intervals. In each panel, the orange line is the average of 20 mock samples, with error bars indicating the standard deviation of individual mock samples around the average. For comparison, the *true* luminosity functions and mass functions estimated directly from the model galaxies in the simulation are plotted as blue triangles connected by blue lines. The limits of the luminosity and stellar mass functions are plotted as black vertical lines. As can be seen, the measurements from the mock catalogs reproduce well the input model results, demonstrating that our weighting scheme to correct the incompleteness effect performs very well.

We use 20 mock samples to estimate the cosmic variance in the stellar mass functions expected from the zCOSMOS survey. For each measurement of the stellar mass function, we obtain the fractional variance among the mock samples, σ_{tot} , which is plotted as error bars in Figure 8. Assuming that the total fractional variance is contributed by cosmic variance and Poisson fluctuations, we can write the total fractional variance as

$$\sigma_{\text{tot}}^2 = \sigma_{\text{cv}}^2 + \sigma_{\text{P}}^2, \quad (15)$$

where σ_{tot} is the total fractional variance for the $\log_{10} M_*$ bin in question, σ_{cv} is the fractional variance due to cosmic

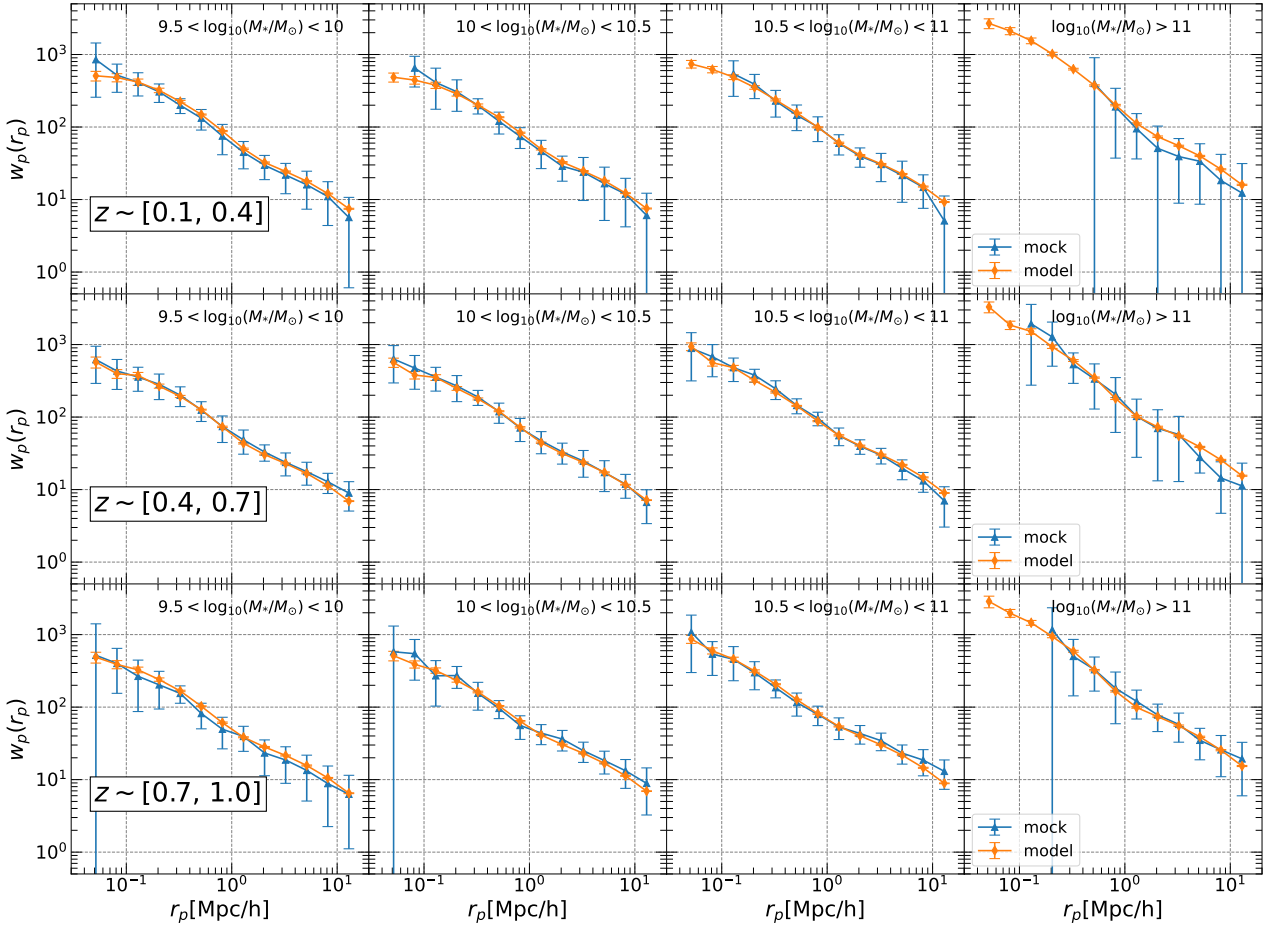


Figure 10. The projected 2PCF $w_p(r_p)$ estimated from the zCOSMOS-bright mock catalogs, for different redshift intervals and different stellar mass M_* bins, as indicated. The effects of sample incompleteness are corrected using our method (see the text for details). In each panel, the orange line is the *true* $w_p(r_p)$ estimated from the model galaxies in the simulation which are used to construct the mock catalogs.

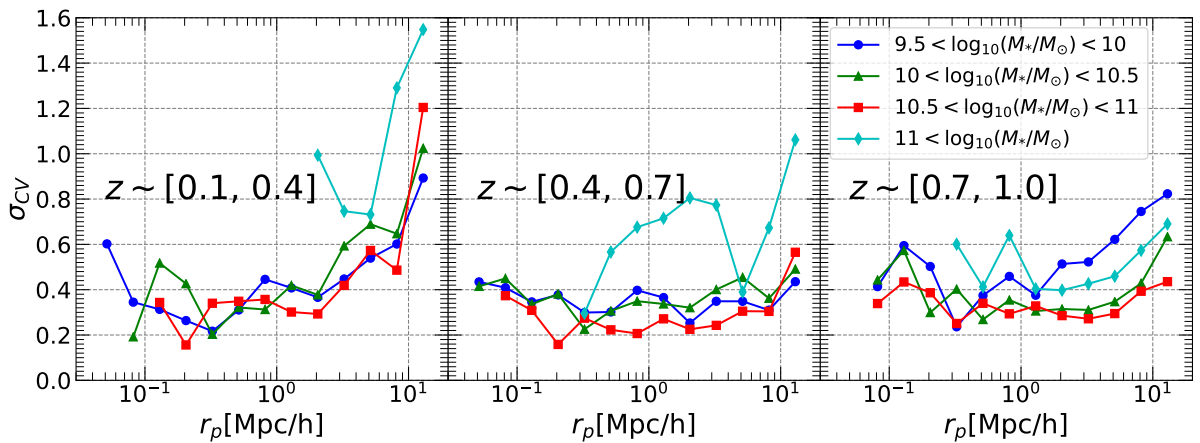


Figure 11. The fractional variance caused by cosmic variance of the projected 2PCF $w_p(r_p)$ estimated for the zCOSMOS-bright survey using mock catalogs, for different redshift intervals and different stellar mass ranges as indicated.

variance, and σ_P is the fractional variance due to Poisson noise given by $\sigma_P = 1/\sqrt{N}$ (with N being the number of galaxies used in the measurement). The cosmic variance of the mass functions for the zCOSMOS survey is shown in Figure 9 as a function of mass and for different redshift bins. The cosmic variance causes a fractional variance of up to 10%-20% at $10^{9.5}M_\odot \lesssim M_* \lesssim 10^{10.5}M_\odot$, and 20%-30% at both higher and lower masses. This result is in broad agreement with that of Ilbert et al. (2013) who estimated the cosmic variance in their mass function measurements using the public tool `getcv` provided by Moster et al. (2011).

Chen et al. (2019) obtained an empirical formula for estimating the cosmic variance as function of stellar mass and survey volume. We plot the σ_{cv} predicted by this formula as the lines of different styles in Figure 9. The trend of the cosmic variance with stellar mass is similar to that from the mock catalogs, in the sense that σ_{cv} decreases slightly with increasing mass, before increasing again when M_* exceeds $\sim 10^{11}M_\odot$. However, the empirical formula overpredicts the σ_{cv} at fixed mass, particularly at low redshifts. This may be understood from the different shape of the survey volume considered in Chen et al. (2019). Those authors used a cubic simulation box to estimate the cosmic variance, while zCOSMOS is a pencil-beam survey. Driver & Robotham (2010) find that a survey in a long and thin volume has a smaller cosmic variance than a survey in a spherical volume. Therefore the formula in Chen et al. (2019) actually gives an upper limit of the cosmic variance for real surveys of a given volume.

5.2 The Projected Two-point Correlation Function

We use the method described in § 4.1.2 to construct the random sample and measure the projected 2PCF for the mock catalogs of zCOSMOS. The zCOSMOS survey uses the *I*-band apparent magnitude to select the targets and the magnitude limit is $I_{lim} = 22.5$. We also apply the correction of the sampling rate effect with the weighting $w_{sky,i}$ and the correction of the fiber collision effect with the angular correlation function to the projected 2PCF. Figure 10 displays the measurements of $w_p(r_p)$ from the mock catalogs in different intervals of redshift and stellar mass. For comparison, the *true* $w_p(r_p)$ estimated directly from the model galaxies in the simulation is also plotted. We choose 12 different line-of-sight directions in the simulation and estimate $w_p(r_p)$ for each of them. We then take the average of the 12 estimates as the *true* $w_p(r_p)$ of the model galaxies, and estimate its error by the standard deviation of the 12 estimates, which is plotted as error bars. As can be seen, the $w_p(r_p)$ measurements from the mock catalogs reproduce the clustering of the model galaxies very well, and this is true for all masses and redshifts. This demonstrates that our correction methods and the method of measuring the correlation functions work well for incomplete spectroscopic surveys like the zCOSMOS.

We use the 20 mock catalogs to estimate the effect of cosmic variance on the measurement of $w_p(r_p)$. As in the previous subsection, we assume the total fractional variance among the 20 mock samples σ_{tot} is a combined effect of the cosmic variance σ_{cv} and the Poisson noise σ_P (Equation 15). We also assume that the Poisson noise only

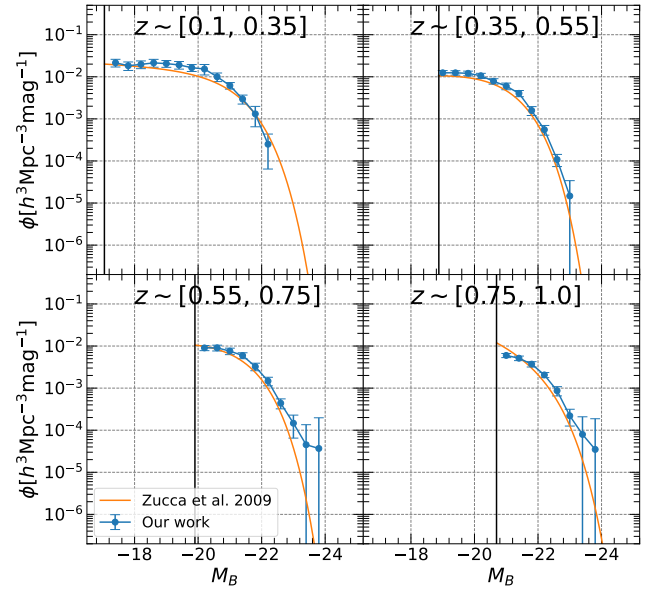


Figure 12. The blue lines represent the *B*-band luminosity function estimated using our method from the real data of the zCOSMOS-bright sample. The error bars are estimated using the method in § 5.3. The orange lines are the previous measurements from Zucca et al. (2009). The black vertical lines indicate the lower limit of M_B due to the limited depth of the survey.

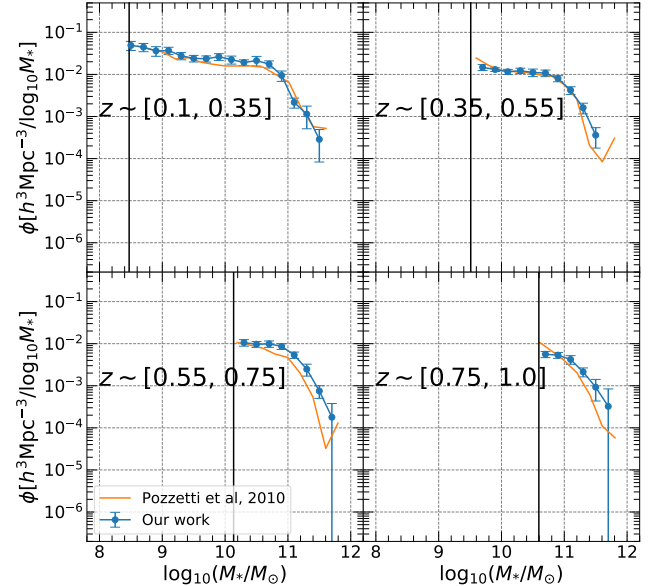


Figure 13. The blue lines represent the galaxy stellar mass function estimated using our method from the real zCOSMOS-bright sample. The error bars are estimated using the method in § 5.3. The orange lines are the previous measurements from Pozzetti et al. (2010). The black vertical lines indicate the lower limit due to the limited depth of the survey.

comes from fluctuations in the galaxy-galaxy pair counts in Equation 8. In this case the fractional variance of $w_p(r_p)$ due to Poisson noise is given by $\sigma_P = 1/\sqrt{DD_p(r_p)}$, where $DD_p(r_p)$ is the number of galaxy-galaxy pairs at r_p , that is, $DD_p(r_p) = \sum_{i=1}^n DD(r_p, \pi_i)$. The cosmic variance of $w_p(r_p)$ so obtained is shown in Figure 11, for the same redshift and stellar mass intervals as in the previous figure. Overall, the relative error of $w_p(r_p)$ caused by the cosmic variance is about 20-40% at $r_p \lesssim 1\text{Mpc}/h$ and increases to above 50% at larger scales. The cosmic variance increases with r_p , and the effect is stronger at lower redshifts. The cosmic variance appears to decrease slightly with increasing mass at $M_* < 10^{11} M_\odot$, while the sub-sample of the highest mass shows larger variance than most of the other sub-samples.

In § 4.2 we mention that a galaxy sample selected by a flux criterion can cause bias in the correlation function. The results shown in Figure 10 indicate that such bias is not important for the zCOSMOS sample, as the measurements without correcting the flux limit effect reproduce well the input results. This will also be seen in the real data of zCOSMOS in the following subsection (Figure 15). However, as we will show in § 6.2, the flux limit effect is significant for low-mass red galaxies at high redshift in the PFS survey.

5.3 The Application to The Real zCOSMOS Sample

Now we apply our methods to the real data of the 20k zCOSMOS-bright sample (called zCOSMOS sample in the following) to measure the stellar mass function and the projected 2PCF. Spectroscopic redshifts for galaxies are provided by the zCOSMOS data release. We only use galaxies with reliable redshifts with confidence classes 1.5, 2.4, 2.5, 9.3, 9.5 3.x, and 4.x Lilly et al. (2009), in the central region of the survey, $149.62^\circ < \text{R.A.} < 150.61^\circ$ and $1.75^\circ < \text{DEC.} < 2.70^\circ$. The sample consists of 11458 galaxies. For each galaxy in the sample we have estimated a stellar mass based on the multi-band spectral energy distribution (SED) taken from the COSMOS2015 catalog (Laigle et al. 2016). For this purpose, we match the galaxies in the zCOSMOS sample with objects in the COSMOS2015 catalog according to sky coordinates, and all the galaxies in zCOSMOS have counterparts in COSMOS2015. With the multi-band photometric data and the redshift, we perform a SED fitting for each galaxy using CIGALE (Boquien et al. 2019). The fitting uses the Stellar Population Synthesis (SPS) model of BC03 (Bruzual & Charlot 2003), a star formation history model given by $\text{SFR}(t) \propto t \exp(-t/\tau)$, the Chabrier initial mass function (Chabrier 2003), and spectral templates with metallicities $Z = 0.0001, 0.004, 0.02, \text{ and } 0.05$. For the attenuation curve, we adopt the `dustatt_modified_staburst` module in CIGALE, which is based on the models of Calzetti et al. (2000) and Leitherer et al. (2002). We also add the nebular emission module as described in Boquien et al. (2019).

The parent photometric sample for the zCOSMOS sample is defined by all the galaxies with $I < 22.5$ in the COSMOS2015 catalog. Using the scheme described in § 4.3.1, we obtain the weight, $w_{\text{sky},i}$, for each galaxy in the zCOSMOS sample. The stellar mass function, luminosity function and projected correlation function can then be estimated in the same way as described in the last two subsections.

The rest-frame B -band luminosity functions are shown

in Figure 12 as blue lines. The fractional variances are obtained using Equation 15, where the σ_{cv} is adopted from the mock catalogs in § 5.1 and the N in σ_P is the number of galaxies in the real sample. The error bars are calculated by multiplying the fractional variance σ_{tot} and LF. For comparison, the orange lines are the results obtained by Zucca et al. (2009) from the 10k zCOSMOS-Bright sample using the *STY* method (Sandage et al. 1979) and assuming a Schechter function (Schechter 1976). Overall, our results are consistent with theirs. The stellar mass functions are shown in Figure 13. Here again blue lines are our results, with error bars obtained with the same method for luminosity function described above. The orange lines are the results obtained by Pozzetti et al. (2010) from the 10k zCOSMOS-Bright sample using the V_{max} method. At high redshift, the stellar mass function we obtain is higher than that of Pozzetti et al. (2010). This discrepancy may be produced by the different SED-fitting codes to measure the stellar mass. The SED fitting code used in Pozzetti et al. (2010) is *Hyperzmass* (Pozzetti et al. 2007), which uses the Calzetti et al. (2000) extinction law, instead of the extinction law which combines Calzetti et al. (2000) and Leitherer et al. (2002) in the SED-fitting model adopted here. They only adopt the solar metallicity, but we use a set of value of metallicities in the SED-fitting code we use. There is also the nebular emission module in (Pozzetti et al. 2007). The uncertainty in SED fitting is larger at higher redshift, because the observational bands correspond to bluer rest-frame bands.

The projected 2PCFs in different redshift intervals are shown in Figure 14. In each panel, different lines represent $w_p(r_p)$ for different stellar mass bins. The fractional variance are obtained using Equation 15, where the σ_{cv} is adopted from the mock catalogs in § 5.2 and the $DD_p(r_p)$ is estimated from the real sample with the same method in § 5.2. The error bars are calculated by multiplying the fractional variance σ_{tot} and $w_p(r_p)$. At given redshift, the correlation functions have similar shape and the amplitude at given scale increases with stellar mass. This is broadly consistent with previous results of galaxy clustering at both low redshift (e.g. Li et al. 2006b; Zehavi et al. 2011) and high redshift (e.g. Meneux et al. 2009). In Figure 15, we compare our results with those of Meneux et al. (2009) obtained from the 10k zCOSMOS-Bright sample for galaxies with $0.8 < z < 1$. The two sets of measurements are consistent with each other on small scales. There is some discrepancy on scales larger than $1\text{Mpc}/h$, although the difference is not large in comparison to the errors. We also attempt to correct potential bias caused by the flux limit effect in the zCOSMOS sample, and find no significant changes in our results, as shown in the blue symbols/lines in the same figure.

For reference, we list our measurements of the luminosity functions, stellar mass functions, and the projected 2PCFs in Table C1, Table C2 and Table C3 in Appendix C.

6 NUMBER DENSITY AND CLUSTERING OF GALAXIES IN PFS GALAXY EVOLUTION SURVEY

In this section, we measure the abundance and clustering of galaxies in the mock catalogs we construct in § 3 for the PFS galaxy evolution survey. The purpose is two-fold. First, we

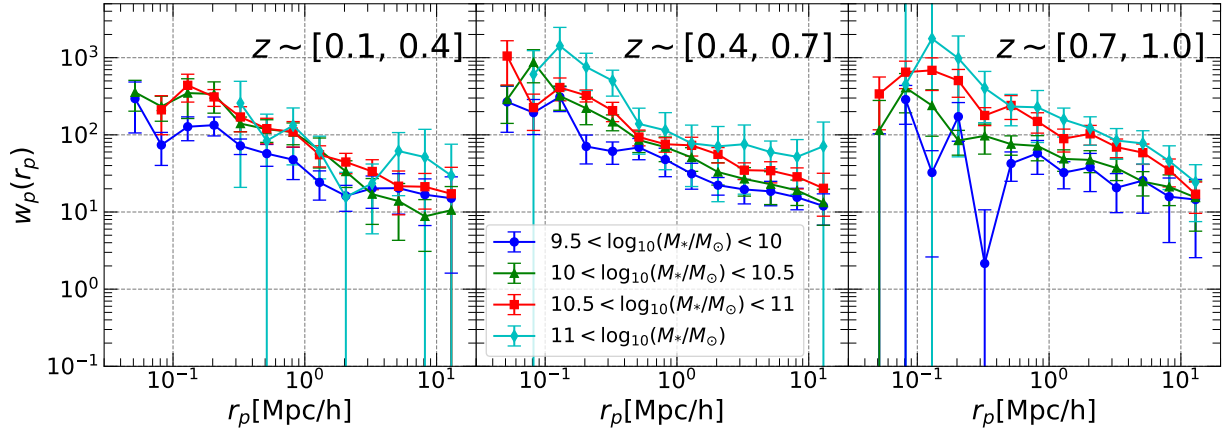


Figure 14. The projected 2PCF $w_p(r_p)$ measured from the real zCOSMOS-bright sample in different redshift intervals and different stellar mass bins, using our method detailed in the text. Error bars are estimated using the method in § 5.3.

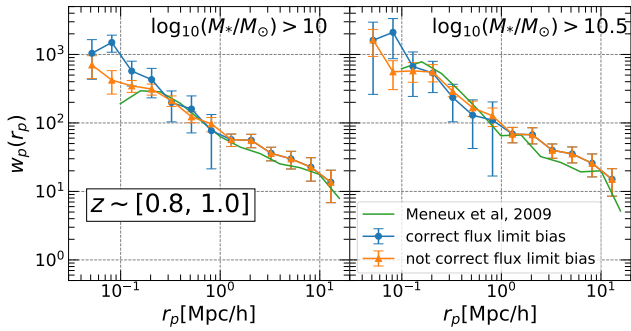


Figure 15. The projected 2PCF $w_p(r_p)$ measured from the real zCOSMOS-bright sample, for two subsamples selected by stellar mass threshold as indicated. The blue symbols/lines present the *correct* measurements for which we have corrected all the sample incompleteness effects including the bias caused by the flux limit of the survey (see text in § 4.3.3). The orange symbols/lines are the measurements that are not corrected for the flux limit bias. The green lines are the measurements from Meneux et al. (2009). Errors of our measurements are estimated using the method described in § 5.3.

use the mock catalogs to test our measuring method of number density and clustering for the PFS survey, as we did for the zCOSMOS in the previous section. Second, we use the mock catalogs to estimate the errors in the measurements and make comparisons with those obtained from the zCOSMOS sample. This allows us to predict the improvements of the upcoming PFS survey relative to existing surveys, such as the zCOSMOS.

6.1 Galaxy Luminosity and Stellar Mass Functions

We first estimate the y -band luminosity function and stellar mass function for the PFS galaxy mock sample, using the same V_{\max} -weighting method in § 4.1.1. Different from the zCOSMOS, which uses a single magnitude limit for the sample selection, the PFS sample will be selected by two magnitude limits: $y < 22.5$ for $0.7 < z < 1$, and $J < 22.8$ for

$1 < z < 1.7$. We estimate a maximum volume for both limits, $V_{\max,y}$ and $V_{\max,J}$, use the larger one as the actual V_{\max} : $V_{\max} = \text{Max}\{V_{\max,y}, V_{\max,J}\}$. We also use the algorithm based on Voronoi tessellation to estimate the sky position-dependent sampling rate, f_s (RA, Dec), as described in § 4.3.1, and we assume a fixed success rate, $f_z = 1$, for redshift determinations. In reality, f_z is smaller than one and may depend on galaxy properties and redshift. The actual value of f_z will be implemented in the future when real data from the PFS survey become available. The total weight for each galaxy in the mock sample is then given by Equation 11, and is used to weight the galaxy when we estimate the luminosity function and stellar mass function.

The y -band luminosity function and stellar mass function obtained this way are shown in Figure 16 and Figure 17, respectively. Panels from left to right are the results for three different redshift intervals: $0.7 < z < 1$, $1 < z < 1.4$ and $1.4 < z < 1.7$. As above, we take the average of the 20 mock catalogs as our mean measurements and their standard deviation as the errors. The *true* luminosity function and mass function measured from the model galaxies in the simulation are plotted for comparison. As can be seen, the measurements obtained using our weighting scheme can well reproduce the input luminosity function and stellar mass function.

The black vertical line in each panel indicates the limiting luminosity ($M_{y,\text{lim}}$) or the limiting mass ($M_{*,\text{lim}}$) to which these two functions can be measured with the PFS sample. The limit for the luminosity function at a given redshift is determined by the apparent magnitude limit, which is either $y < 22.5$ or $J < 22.8$. For the mass function, we calculate two $M_{*,\text{lim}}$ for each galaxy using Equation 7 — one for $y_{\text{lim}} = 22.5$ and the other for $J_{\text{lim}} = 22.8$, and we use the larger one of the two as the actual limit for the galaxy. The mass limit for the mass function is then determined in the same way as in § 4.1.1.

Figure 18 shows the cosmic variance, σ_{cv} , in the stellar mass function expected from the PFS galaxy sample, estimated from the 20 mock catalogs in the same way described in § 5.1. The σ_{cv} is plotted as a function of the number of PFS pointings, each covering 1.3 deg^2 , and for different stellar mass and redshift intervals. For comparison, the σ_{cv}

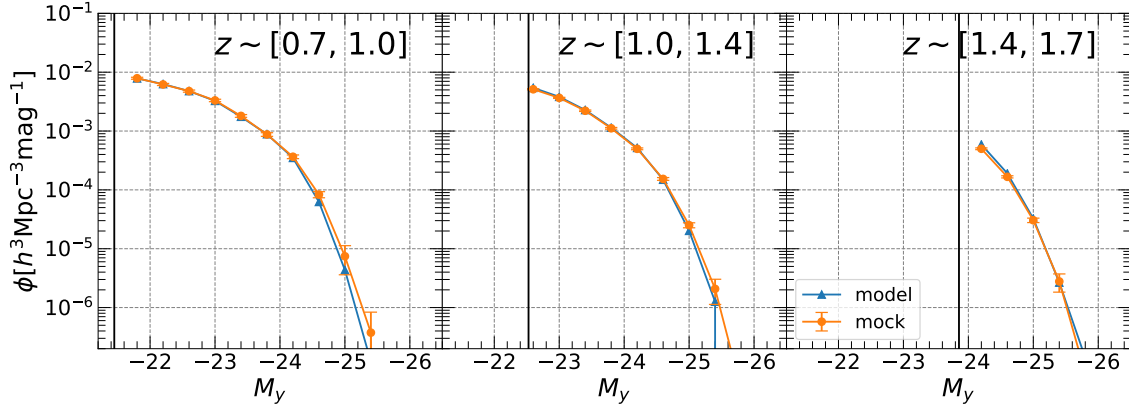


Figure 16. The y -band luminosity function estimated from the mock catalogs of the PFS galaxy survey is plotted as orange dots, and is compared to the *true* luminosity function of model galaxies in the simulation. Results are shown for three different redshift intervals as indicated. The black vertical line in each panel indicates the sample limit.

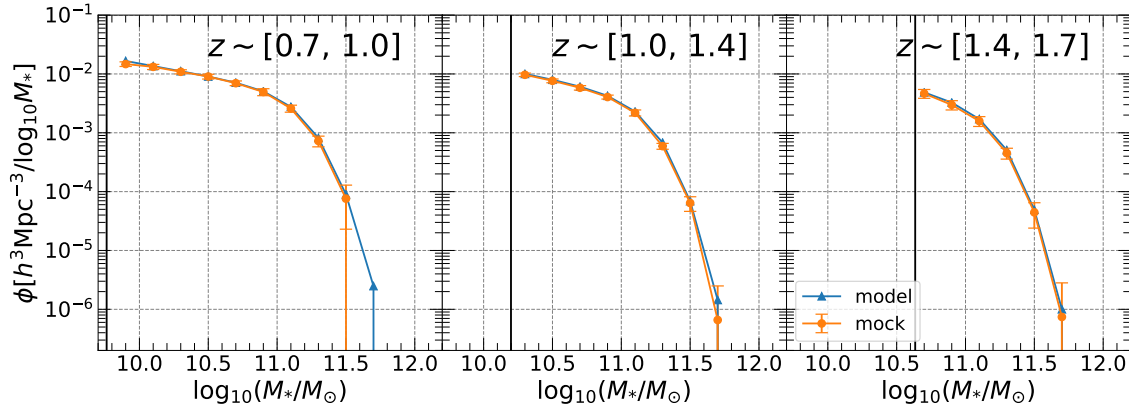


Figure 17. The galaxy stellar mass function estimated from the mock catalogs of the PFS galaxy survey is plotted as orange dots, and is compared to the true luminosity function of model galaxies in the simulation. Results are shown for three different redshift intervals as indicated. The black vertical line indicates the sample limit.

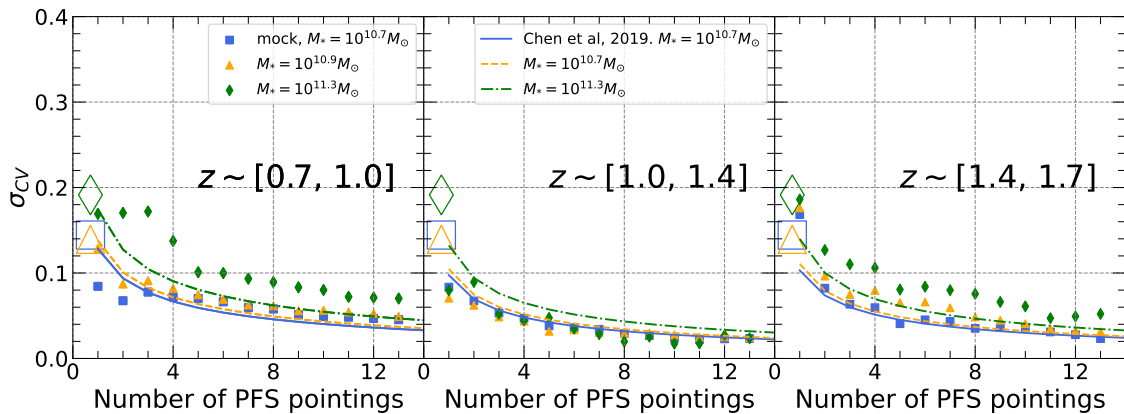


Figure 18. The fractional variance caused by cosmic variance of the stellar mass function is estimated from the mock catalogs of the PFS galaxy survey, as a function of the number of the PFS pointings (each covering 13 deg^2 in the sky). Results are shown for different redshift intervals in different panels, and in each panel the different symbols/colors are for different stellar masses as indicated. The large symbols are the cosmic variance estimated for the zCOSMOS-bright survey. The lines represent the predictions by the empirical formula of Chen et al. (2019).

estimated for the zCOSMOS sample in the previous section are plotted as the big symbols. Overall, as expected, the cosmic variance in the galaxy mass function decreases rapidly with increasing area of the survey. When compared to the zCOSMOS, the error caused by the cosmic variance is expected to decrease from 10%-20% to 3%-5% for the complete PFS survey. At a fixed survey area, the cosmic variance shows weak dependence on mass for the two lower mass bins, but it increases dramatically for the highest mass bin. The empirical formula obtained by Chen et al. (2019) are also plotted. As can be seen, the trends of the cosmic variance with both survey area and mass are roughly consistent with the formula.

6.2 The projected Two-point Correlation Function

Now we measure the projected 2PCF $w_p(r_p)$ for the PFS mock sample, and again we start by constructing a random sample that has the same selection effects as the mock sample. Our method for constructing the random sample has been detailed in § 4.1.2. A specific treatment for the case here is that we have to assign luminosities in both y -band and J -band to the galaxies in the random sample (called random galaxies). First, we use the y -band luminosity function derived in § 6.1 to assign a y -band absolute magnitude to each random galaxy. Then, we assign to each random galaxy a stellar mass according to the M_y - M_* relation in the mock sample. To this end, we divide galaxies in both the mock and random samples into successive bins of M_y with a fixed width of 0.2 dex. In each M_y bin, we fit the distribution of the M_* in the mock sample with a Gaussian, according to which we randomly assign a stellar mass to a galaxy in the random sample contained in the same M_y bin. Next, for each random galaxy, we randomly pick a galaxy in the same M_y bin from the mock sample and assign its rest-frame $y - J$ color and the k -corrections, K , in both the y -band and J -band to the random galaxy. Finally, we calculate the apparent magnitudes, m_y and m_J , for all random galaxies. The final random sample is selected as random galaxies that satisfy the apparent magnitude criteria of the PFS survey.

We estimate the projected 2PCF $w_p(r_p)$ for the PFS mock sample using the same estimator in § 4.1.2 and we correct for the sampling rate effect, the fiber collision effect and flux limit effect using our methods detailed in § 4.3. The results are shown in Figure 19 as blue symbols/lines (labelled as corrected w_{pp}). Again, as above, the mean measurement of $w_p(r_p)$ is given by the average of the 20 mock samples, while the error at a given r_p is estimated by the standard deviation of the mock samples around the average. For comparison, the *true* $w_p(r_p)$ of galaxies in the same mass and redshift bins are obtained from the model galaxies in the simulation and are plotted as the green symbols/lines. In all cases, the measured $w_p(r_p)$ match the true $w_p(r_p)$ very well.

In order to highlight the flux limit effect, we have constructed a set of “100% complete” mock catalogs that are exactly the same as the mock sample of the PFS except that the sampling rate is set to 100%. As can be seen from Figure 19, the $w_p(r_p)$ of the complete (100%) sample so obtained is significantly lower than the true $w_p(r_p)$ at scales smaller than a few Mpc. This effect is seen mainly in the

lowest mass bin with $10 < \log_{10}(M_*/M_\odot) < 10.5$, and is stronger at higher redshifts. In Figure 20 we show the same comparison for the mass range of $10 < \log_{10}(M_*/M_\odot) < 10.5$ again, but now separately for red and blue galaxies. Clearly, the underestimation of the small-scale clustering seen in the total (red plus blue) sample is contributed only by red galaxies. This is expected, because low-mass red galaxies have a higher probability to be excluded from the sample due to their higher mass-to-light ratios than their blue counterparts. Low-mass red galaxies are also strongly clustered (e.g. Li et al. 2006b,a, 2007; Zehavi et al. 2011) and more likely satellite galaxies in massive halos (e.g. Li et al. 2006a, 2007; Lan et al. 2016), so that the reduction of this population in the sample can lead to an underestimate of the correlation function on small scales.

It is encouraging that the $w_p(r_p)$ measurements including the correction for all the three effects (the blue symbols/lines match the true $w_p(r_p)$ very well). This demonstrates that our method is powerful in correcting the bias caused by flux selection criteria.

6.2.1 Cosmic variance in the 2PCF

Finally, we show the cosmic variance in the 2PCF as a function of the number of PFS pointings in Figure 21, for galaxies of different mass and redshift. The σ_{cv} are obtained using the 20 mock catalogs, in the same way as in the previous section except that the $w_p(r_p)$ are measured using the method described above. For comparison, the cosmic variances estimated for the zCOSMOS survey are plotted as the large symbols. We can see that the cosmic variance is the smallest at the intermediate scale and is bigger at both larger and smaller scales. The cosmic variance increases with stellar mass, but at fixed mass and scale it decreases with the survey area, as expected. Compared with the zCOSMOS survey, the cosmic variance expected from the PFS survey is about a factor of ~ 3 smaller.

7 SUMMARY

In this paper we studied the abundance and clustering of galaxies at high redshift as function of luminosity, stellar mass and redshift, using realistic mock catalogs constructed from cosmological simulations. We populated the halos and subhalos of dark matter in the simulation with model galaxies of different masses and colors. We calibrate the galaxy model using multi-band deep imaging data from COSMOS2015. We then constructed mock catalogs for spectroscopic surveys based on the model galaxies in the simulation. We considered two multi-object spectroscopic surveys: one is the existing zCOSMOS survey, and the other is the upcoming PFS galaxy evolution survey. When constructing the mock catalogs, we carefully included the same selection effects as the real surveys. These include the area/redshift boundaries, the incomplete sampling due to the limited number of fibers/slits and the fiber/slit collision effects, and sample selection by flux criteria. Using the mock catalogs we measured the luminosity function (LF), stellar mass function (SMF), and projected two-point correlation function (2PCF) for galaxies of different stellar mass at different redshift. For the zCOSMOS survey, we further apply our method to the

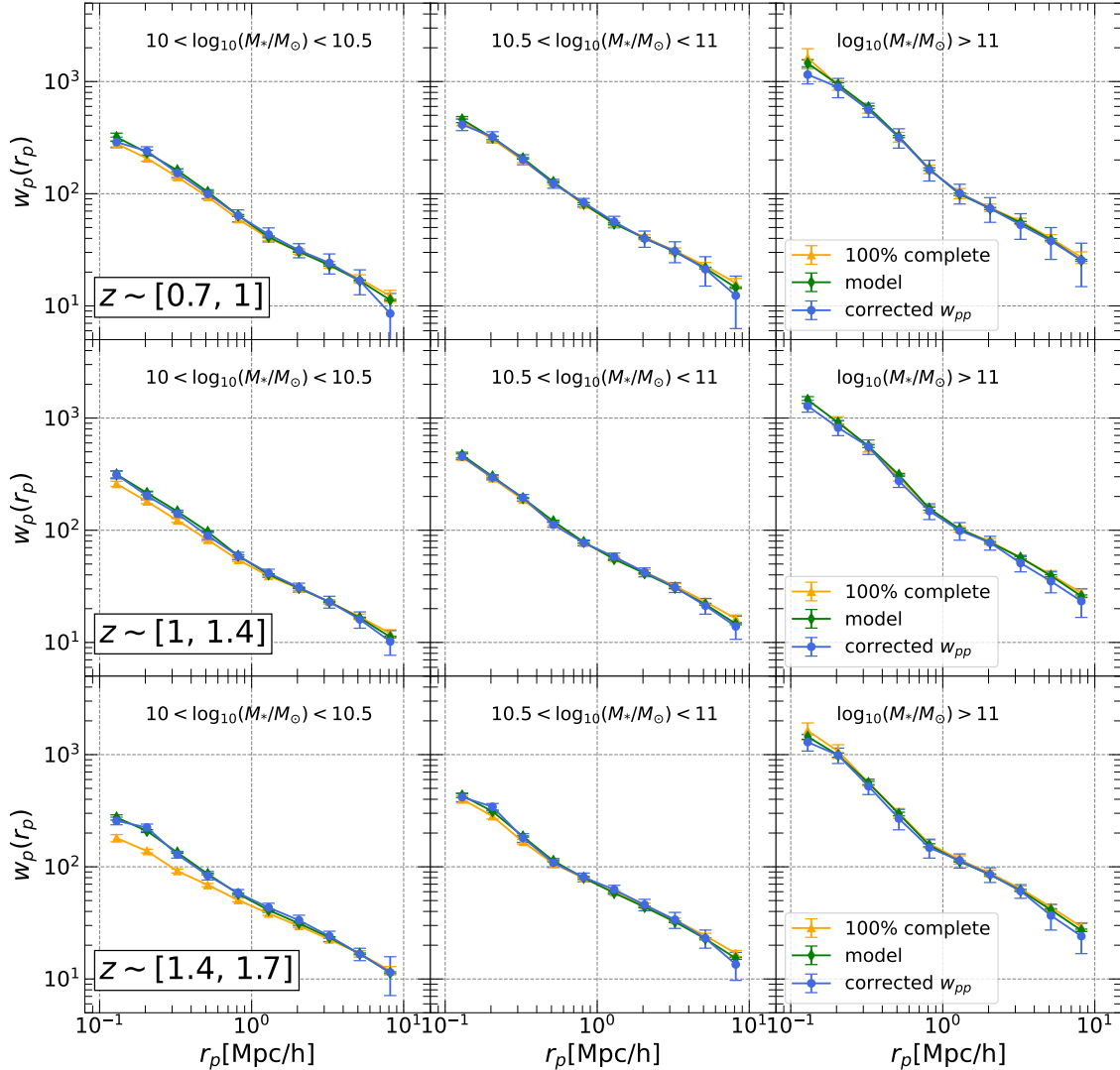


Figure 19. The projected 2PCF $w_p(r_p)$ measured from the mock catalogs of the PFS galaxy survey, for different redshift intervals and different stellar mass ranges, as indicated. The blue symbols/line present the *correct* measurements for which we have corrected all the sample incompleteness effects including the bias caused by the flux limit of the survey (see text in § 4.3.3. The orange symbols/line are measured from the 100% complete mock catalogs with a sample rate of 100%, but are not corrected for the flux limit bias. The green symbols/line are the true $w_p(r_p)$ estimated directly from the model galaxies in the simulation.

real data and make comparison with previous measurements from the literature.

We found that incomplete sampling can lead to significantly biased measurements of galaxy luminosity/stellar mass function. We applied a weighting scheme to explicitly account for the sky position-dependent sampling rate, and our test with the mock catalogs showed that the bias caused by the incomplete sampling can be well corrected for the luminosity/stellar mass functions for both zCOSMOS (Figure 7, Figure 8) and PFS (Figure 16, Figure 17). Our measurements of the luminosity function and mass function from the real data of zCOSMOS are also in good agreement with previous measurements (Figure 12, Figure 13).

For galaxy clustering, we found that both the target selection by flux criteria and the incomplete sampling can lead to significantly biased measurements. The effect of incomplete sampling can be fully corrected using our weighting

scheme and the correction of fiber/slit collision (Figure 10), but the bias due to the selection criteria of flux-limited samples cannot be corrected in a simple way. This bias is more significant at lower masses and at higher redshifts, and is mainly contributed by the population of low-mass red galaxies which are more strongly clustered but less well sampled due to their larger mass-to-light ratios in comparison to blue galaxies. We developed a new method to correct this bias, with the help of two photometric samples from the parent sample. We showed that the bias in the projected $w_p(r_p)$ can be almost perfectly corrected with this method, for all the stellar mass and redshift considered (Figure 19, Figure 20). This bias is weak for the zCOSMOS survey because it is at relatively low redshift, although our correction method still works well in this case (§ 5.2).

We used the mock catalogs to estimate the effect of cosmic variance in both the abundance and clustering measure-

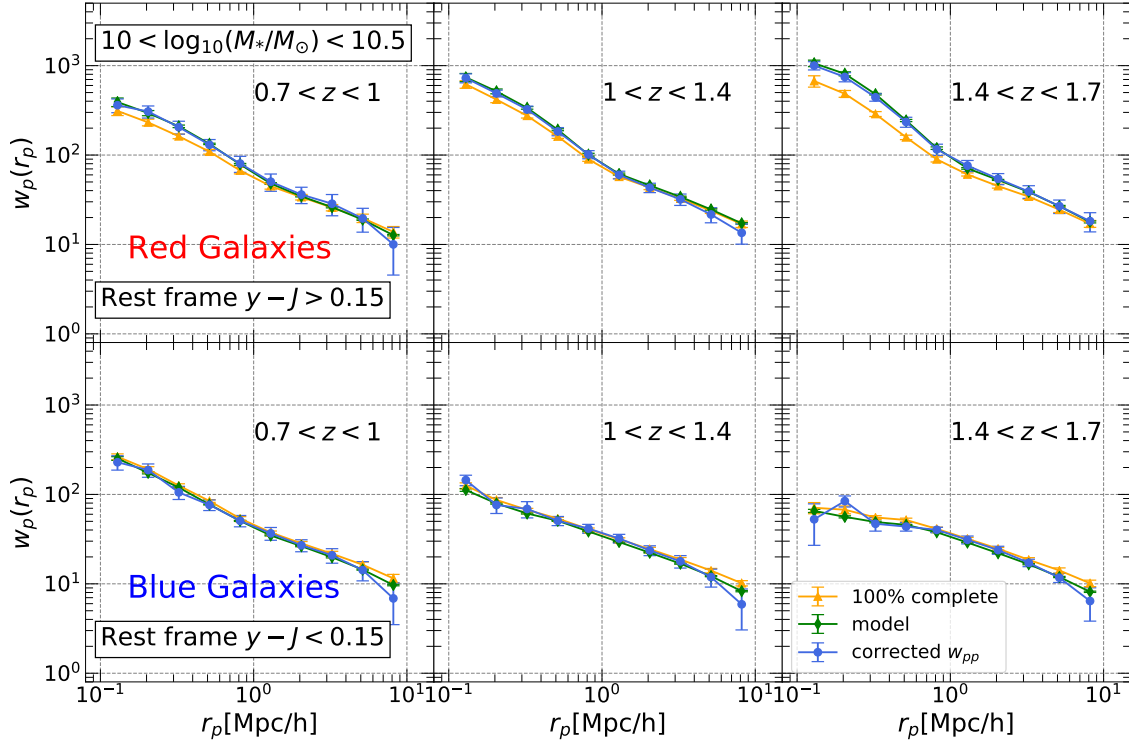


Figure 20. Measurements of $w_p(r_p)$ for the subset of red galaxies (upper panels) and blue galaxies (lower panels) in different redshift ranges as indicated, using the PFS mock catalogs with stellar mass limited to $10 < \log_{10} M_*/M_\odot < 10.5$. Symbols/lines/colors are the same as in the previous figure.

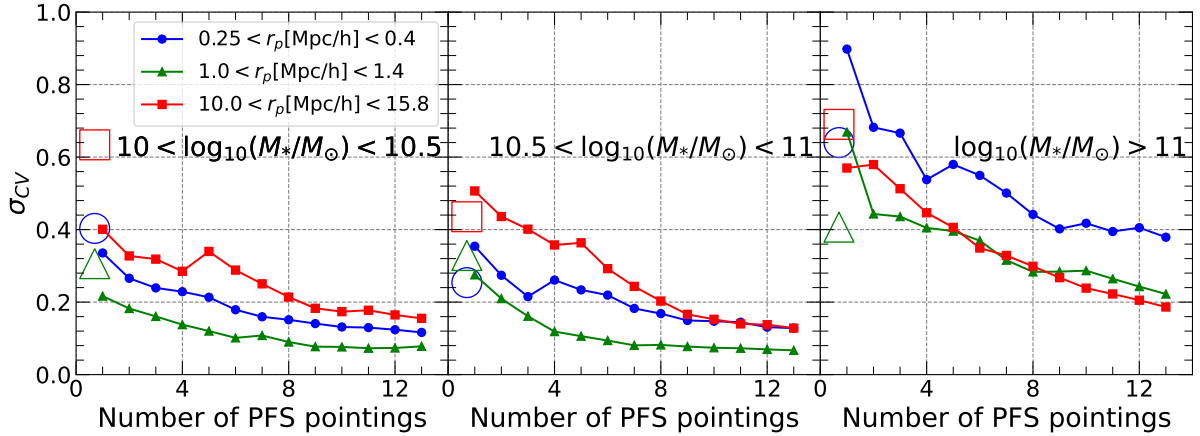


Figure 21. The fractional variance caused by cosmic variance for projected 2PCF as a function of the number of the PFS pointings (each covering 13 deg^2), for different redshift intervals and different stellar mass ranges, as indicated. The large symbols are the cosmic variance estimated for the zCOSMOS-bright survey.

ments, and we made comparisons between zCOSMOS and the PFS galaxy survey. For the stellar mass function, we found that the relative error caused by the cosmic variance, σ_{cv} , decreases with survey area, from 10-20% in zCOSMOS-like surveys that have a survey area of $\sim 1 \text{ deg}^2$ down to 2-5% in PFS-like surveys that covers $\sim 14.5 \text{ deg}^2$ (Figure 18). For the projected 2PCF, the cosmic variance also decreases with survey area, but differently for galaxies of different mass, with the change being more significant at higher mass. On average, the relative error of $w_p(r_p)$ expected from PFS is

reduced by a factor of 3 relative to that from zCOSMOS (Figure 21). Overall, our results show that both statistical uncertainties and the cosmic variance for both the abundance and clustering measurements can be reduced significantly in the PFS galaxy survey in comparison to those in existing surveys, and that unbiased measurements can be obtained using the methods developed here.

ACKNOWLEDGEMENTS

This work is supported by the National Key R&D Program of China (grant No. 2018YFA0404502, 2018YFA0404503), and the National Science Foundation of China (grant Nos. 11821303, 11973030, 11673015, 11733004, 11761131004, 11761141012). Part of our analysis is based on data products from observations made with ESO Telescopes at the La Silla Paranal Observatory under ESO programme ID 179.A-2005 and on data products produced by TERAPIX and the Cambridge Astronomy Survey Unit on behalf of the UltraVISTA consortium.

REFERENCES

- Abbas U., Sheth R. K., 2006, *MNRAS*, **372**, 1749
- Aihara H., et al., 2018, *PASJ*, **70**, S4
- Artale M. C., et al., 2017, *MNRAS*, **470**, 1771
- Baldry I. K., Glazebrook K., Driver S. P., 2008, *MNRAS*, **388**, 945
- Baldry I. K., et al., 2012, *MNRAS*, **421**, 621
- Behroozi P. S., Wechsler R. H., Wu H.-Y., Busha M. T., Klypin A. A., Primack J. R., 2013, *ApJ*, **763**, 18
- Bell E. F., McIntosh D. H., Katz N., Weinberg M. D., 2003, *ApJS*, **149**, 289
- Blaizot J., Wadadekar Y., Guiderdoni B., Colombi S. T., Bertin E., Bouchet F. R., Devriendt J. E. G., Hatton S., 2005, *MNRAS*, **360**, 159
- Boquien M., Burgarella D., Roehlly Y., Buat V., Ciesla L., Corre D., Inoue A. K., Salas H., 2019, *A&A*, **622**, A103
- Bottini D., et al., 2005, *PASP*, **117**, 996
- Bruzual G., Charlot S., 2003, *MNRAS*, **344**, 1000
- Bundy K., Conselice C., Ellis R., Eisenhardt P., DEEP2 Team 2003, in American Astronomical Society Meeting Abstracts. p. 106.06
- Calzetti D., Armus L., Bohlin R. C., Kinney A. L., Koornneef J., Storchi-Bergmann T., 2000, *ApJ*, **533**, 682
- Chabrier G., 2003, *PASP*, **115**, 763
- Chen Y., Mo H. J., Li C., Wang H., Yang X., Zhou S., Zhang Y., 2019, *ApJ*, **872**, 180
- Coil A. L., Newman J. A., Cooper M. C., Davis M., Faber S. M., Koo D. C., Willmer C. N. A., 2006, *ApJ*, **644**, 671
- Cole S., Lacey C. G., Baugh C. M., Frenk C. S., 2000, *MNRAS*, **319**, 168
- Cole S., et al., 2001, *MNRAS*, **326**, 255
- Davidzon I., et al., 2013, *A&A*, **558**, A23
- Diener C., et al., 2013, *ApJ*, **765**, 109
- Driver S. P., Robotham A. S. G., 2010, *MNRAS*, **407**, 2131
- Dunkley J., et al., 2009, *ApJS*, **180**, 306
- Farrow D. J., et al., 2015, *MNRAS*, **454**, 2120
- Hawkins E., et al., 2003, *MNRAS*, **346**, 78
- Hearin A. P., Watson D. F., 2013, *MNRAS*, **435**, 1313
- Ilbert O., et al., 2005, *A&A*, **439**, 863
- Ilbert O., et al., 2006, *A&A*, **457**, 841
- Ilbert O., et al., 2013, *A&A*, **556**, A55
- Jing Y. P., Mo H. J., Börner G., 1998, *ApJ*, **494**, 1
- Knobel C., et al., 2012, *ApJ*, **753**, 121
- Komatsu E., et al., 2009, *ApJS*, **180**, 330
- Laigle C., et al., 2016, *ApJS*, **224**, 24
- Lan T.-W., Ménard B., Mo H., 2016, *MNRAS*, **459**, 3998
- Landy S. D., Szalay A. S., 1993, *ApJ*, **412**, 64
- Leitherer C., Li I. H., Calzetti D., Heckman T. M., 2002, *ApJS*, **140**, 303
- Li C., White S. D. M., 2009, *MNRAS*, **398**, 2177
- Li C., Jing Y. P., Kauffmann G., Börner G., White S. D. M., Cheng F. Z., 2006a, *MNRAS*, **368**, 37
- Li C., Kauffmann G., Jing Y. P., White S. D. M., Börner G., Cheng F. Z., 2006b, *MNRAS*, **368**, 21
- Li C., Kauffmann G., Wang L., White S. D. M., Heckman T. M., Jing Y. P., 2006c, *MNRAS*, **373**, 457
- Li C., Jing Y. P., Kauffmann G., Börner G., Kang X., Wang L., 2007, *MNRAS*, **376**, 984
- Lilly S. J., et al., 2007, *ApJS*, **172**, 70
- Lilly S. J., et al., 2009, *ApJS*, **184**, 218
- Lu Y., Mo H. J., Weinberg M. D., Katz N., 2011, *MNRAS*, **416**, 1949
- Lu Z., Mo H. J., Lu Y., Katz N., Weinberg M. D., van den Bosch F. C., Yang X., 2014, *MNRAS*, **439**, 1294
- Lu Z., Mo H. J., Lu Y., Katz N., Weinberg M. D., van den Bosch F. C., Yang X., 2015, *MNRAS*, **450**, 1604
- Madgwick D. S., et al., 2003, *MNRAS*, **344**, 847
- Meneux B., et al., 2009, *A&A*, **505**, 463
- Mo H., van den Bosch F. C., White S., 2010, Galaxy Formation and Evolution
- Mohammad F. G., et al., 2018, *A&A*, **619**, A17
- Moster B. P., Somerville R. S., Newman J. A., Rix H.-W., 2011, *ApJ*, **731**, 113
- Muzzin A., et al., 2013, *ApJS*, **206**, 8
- Norberg P., et al., 2001, *MNRAS*, **328**, 64
- Pollo A., et al., 2006, *A&A*, **451**, 409
- Pozzetti L., et al., 2007, *A&A*, **474**, 443
- Pozzetti L., et al., 2010, *A&A*, **523**, A13
- Sandage A., Tammann G. A., Yahil A., 1979, *ApJ*, **232**, 352
- Schechter P., 1976, *ApJ*, **203**, 297
- Schmidt M., 1968, *ApJ*, **151**, 393
- Shimono A., et al., 2016, in Software and Cyberinfrastructure for Astronomy IV. p. 99133B ([arXiv:1608.01163](https://arxiv.org/abs/1608.01163)), doi:10.1117/12.2232844
- Somerville R. S., Lee K., Ferguson H. C., Gardner J. P., Moustakas L. A., Giavalisco M., 2004, *ApJ*, **600**, L171
- Springel V., et al., 2005, *Nature*, **435**, 629
- Springel V., et al., 2018, *MNRAS*, **475**, 676
- Sunayama T., et al., 2019, arXiv e-prints, p. arXiv:1912.06583
- Takada M., et al., 2014, *PASJ*, **66**, R1
- Wang H., et al., 2016, *ApJ*, **831**, 164
- Wang K., Mo H. J., Li C., Meng J., Chen Y., 2020, arXiv e-prints, p. arXiv:2006.05426
- Wechsler R. H., Tinker J. L., 2018, *ARA&A*, **56**, 435
- Wechsler R. H., Bullock J. S., Primack J. R., Kravtsov A. V., Dekel A., 2002, *ApJ*, **568**, 52
- White S. D. M., Rees M. J., 1978, *MNRAS*, **183**, 341
- Yang X., Mo H. J., van den Bosch F. C., 2003, *MNRAS*, **339**, 1057
- York D. G., et al., 2000, *AJ*, **120**, 1579
- Zehavi I., et al., 2005, *ApJ*, **630**, 1
- Zehavi I., et al., 2011, *ApJ*, **736**, 59
- Zheng Z., et al., 2005, *ApJ*, **633**, 791
- Zucca E., et al., 2009, *A&A*, **508**, 1217
- de la Torre S., et al., 2011, *MNRAS*, **412**, 825

APPENDIX A: SAMPLING RATES VERSUS SURFACE NUMBER DENSITY OF TARGETS

As shown in the main text, the incomplete sampling of galaxy targets in both the zCOSMOS and PFS galaxy samples can well be corrected using our weighting scheme. This is mainly because the sampling rate depends only on the local surface number density of the galaxy targets, although the sampling may vary from region to region. This is demonstrated clearly in Figure A1, where we plot the sky position-dependent sampling rate, $f_s(\text{RA}, \text{Dec})$, in the PFS mock catalogs, defined in § 4.3.1, as a function of the surface density

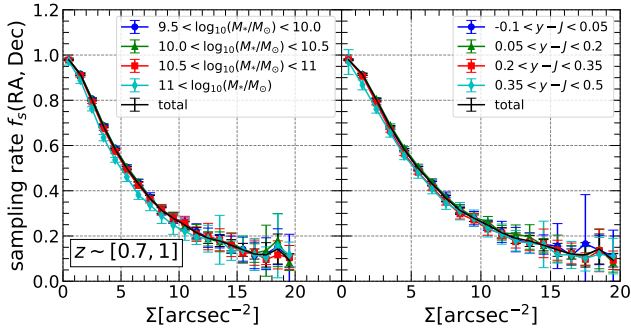


Figure A1. The local sampling rate as a function of the local surface number density of galaxy targets. The colorful lines represent the results for different stellar mass ranges, while the black line is the result for the galaxies as a whole.

Σ . Here, for each galaxy in the mock catalogs, we have estimated a local surface density Σ by counting the number of galaxies in the parent photometric sample that are located within 1 arcmin. We show the sampling rate versus Σ for subsamples selected by stellar mass (left panel) or $y - J$ color (right panel). All the measurements overlap with each other, and are almost the same as the result from the full sample (the black curve), which is the average of the 20 mock catalogs constructed in § 3.

The figure shows that the sampling rate decreases rapidly with Σ , varying from nearly 100% in the lowest density regions down to $\sim 10\%$ in the highest. As shown in the main text, this variation causes large biases in the estimation of the luminosity function, stellar mass function and correlation function. However, our weighting scheme is able to correct these biases for all the statistics even when the sampling rate is very low.

APPENDIX B: METHOD OF MEASURING THE CROSS-CORRELATION FUNCTION BETWEEN SPECTROSCOPIC AND PHOTOMETRIC SAMPLES

In § 4.3.3 we proposed a new method to correct the flux limit bias of the $w_p(r_p)$ measurements, and we showed in § 6.2 that this method works well. The success of this method relies on reliably estimating the two cross-correlation functions: $w_{sp}(r_p)$ and $w_{sp'}(r_p)$, the cross-correlations of the spectroscopic sample (**sample s**) with the parent photometric sample (**sample p**) and with the photometric sample that is selected from **sample p** by the flux criteria but with a 100% sample rate (**sample p'**), respectively.

Here we describe our method for estimating these cross-correlation functions. We use the subscript ‘1’ to represent the sample with spectroscopic redshifts (i.e. **sample s** in our case), and subscript ‘2’ to represent the photometric sample (i.e. **sample p** or **p'**). Given that the projected distance is relatively small compared to the radial distance, the angular separation of a pair of galaxies is small. For a pair of galaxies between the two samples, we can then obtain a project distance from r_1 (the comoving distance corresponding to the redshift of the galaxy in sample 1) according to $r_p = r_1 \sin(\theta) \approx r_1 \theta$, where θ is the angular separation of the pair. The number of pairs between sample 1 and sample

2 with projected separations in $[r_p, r_p + dr_p)$ is thus given by

$$\sum_k w_{sky,k} \times \frac{dN_{k,1}}{2\pi r_p dr_p} = \sum_k w_{sky,k} \times \frac{1}{S} \int_{r_{2,l}}^{r_{2,u}} \left[1 + \xi_{12} \left(\sqrt{r_p^2 + (r_{k,1} - r_2)^2} \right) \right] \frac{dN_2}{dr_2} dr_2. \quad (\text{B1})$$

Here k denotes the k -th galaxy in sample 1; $N_{k,1}$ is the number of galaxies from sample 2 within a projected separation r_p from the k -th galaxy in sample 1; $w_{sky,k}$ is the weight obtained using Equation 10; $r_{2,l}$ and $r_{2,u}$ are, respectively, the lower and upper boundaries of sample 2 in comoving distance; S is the area of the survey at the distance r_1 ; and N_2 is the total number of galaxies in sample 2 within a given distance r_2 . For galaxies in sample 2, we use their photometric redshift (photo- z) to estimate $\frac{dN_2}{dr_2}$. Since ξ_{12} in the integral in Equation B1 decreases rapidly with increasing distance, the corresponding integration is contributed by a narrow interval of r_2 where dN_2/dr_2 is approximately a constant and can be moved out of the integral. The integral is essentially the projected correlation function, as is shown in the following:

$$\begin{aligned} \sum_k w_{sky,k} \times \frac{dN_{k,1}}{2\pi r_p dr_p} &\approx \sum_k w_{sky,k} \times \left[\frac{N_2}{S} + \right. \\ &\quad \left. \frac{1}{S} \frac{dN_2}{dr_2} \int_{r_{2,l}}^{r_{2,u}} \xi_{12} \left(\sqrt{r_p^2 + (r_{k,1} - r_2)^2} \right) dr_2 \right] \\ &= \sum_k \left[\frac{N_2}{S} + \frac{1}{S} \frac{dN_2}{dr_2} w_{12}(r_p) \right]. \end{aligned} \quad (\text{B2})$$

In practice, we estimate $dN_{k,1}$ by counting the cross pairs between **sample s** and a given photometric sample (**sample p** or **p'** in our case here) in $[r_p, r_p + dr_p)$, projecting galaxies in the photometric sample to the radial distance of the spectroscopic sample. We estimate dN_2/dr_2 for the photometric sample. We count the number of galaxies in the photometric sample in the radial distance bins with $\Delta r_2 = 10 \text{ Mpc/h}$ and smooth the radial distribution by a Gaussian kernel with $\sigma = 150 \text{ Mpc/h}$. We have tested several values of σ and found that $\sigma = 150 \text{ Mpc/h}$ is the best choice. Estimates of $w_{sp}(r_p)$ and $w_{sp'}(r_p)$ are then obtained from Equation B2, which are used to estimate the true auto-correlation of the spectroscopic sample, $w_{ss,true}$, according to Equation 14.

APPENDIX C: RESULTS OF GALAXY ABUNDANCE AND CLUSTERING FOR THE ZCOSMOS SAMPLE

In the following tables we list the measurements of the luminosity function (Figure 12), the stellar mass function (Figure 13) and projected 2PCF (Figure 14) obtained with our methods from the 20k zCOSMOS-bright sample, as detailed in § 5.3. The errors are obtained with the method described in § 5.3.

This paper has been typeset from a $\text{\TeX}/\text{\LaTeX}$ file prepared by the author.

Table C1. Measurements of B -band Luminosity Function for the 20k zCOSMOS-bright sample.

M_B	$\log_{10} \Phi(M_B)[h^3\text{Mpc}^{-3}\text{mag}^{-1}]$			
	$0.1 < z < 0.35$	$0.35 < z < 0.55$	$0.55 < z < 0.75$	$0.75 < z < 1$
-17.4	-1.666 ^{+0.082} _{-0.101}			
-17.8	-1.737 ^{+0.089} _{-0.113}			
-18.2	-1.705 ^{+0.082} _{-0.101}			
-18.6	-1.669 ^{+0.084} _{-0.104}			
-19.0	-1.687 ^{+0.073} _{-0.088}	-1.905 ^{+0.053} _{-0.060}		
-19.4	-1.718 ^{+0.081} _{-0.100}	-1.906 ^{+0.050} _{-0.056}		
-19.8	-1.784 ^{+0.075} _{-0.090}	-1.918 ^{+0.052} _{-0.059}		
-20.2	-1.815 ^{+0.107} _{-0.142}	-1.975 ^{+0.057} _{-0.066}	-2.044 ^{+0.057} _{-0.065}	
-20.6	-2.000 ^{+0.090} _{-0.114}	-2.105 ^{+0.060} _{-0.070}	-2.043 ^{+0.063} _{-0.074}	
-21.0	-2.208 ^{+0.071} _{-0.085}	-2.221 ^{+0.072} _{-0.086}	-2.121 ^{+0.070} _{-0.084}	-2.223 ^{+0.046} _{-0.052}
-21.4	-2.528 ^{+0.094} _{-0.120}	-2.393 ^{+0.067} _{-0.080}	-2.225 ^{+0.065} _{-0.077}	-2.289 ^{+0.051} _{-0.057}
-21.8	-2.881 ^{+0.178} _{-0.306}	-2.801 ^{+0.092} _{-0.118}	-2.488 ^{+0.080} _{-0.099}	-2.430 ^{+0.059} _{-0.068}
-22.2	-3.602 ^{+0.241} _{-0.590}	-3.257 ^{+0.100} _{-0.131}	-2.832 ^{+0.090} _{-0.114}	-2.686 ^{+0.056} _{-0.064}
-22.6		-3.965 ^{+0.121} _{-0.168}	-3.358 ^{+0.102} _{-0.134}	-3.062 ^{+0.096} _{-0.124}
-23.0		-4.831 ^{+0.364} _{-4.714}	-3.834 ^{+0.132} _{-0.354}	-3.657 ^{+0.155} _{-0.244}
-23.4			-4.345 ^{+0.476} _{-4.046}	-4.100 ^{+0.419} _{-3.890}
-23.8			-4.433 ^{+0.729} _{-3.794}	-4.456 ^{+0.729} _{-3.817}

Table C2. Measurements of Galaxy Stellar Mass Function for the 20k zCOSMOS-bright sample.

$\log_{10} M_* [M_\odot]$	$\log_{10} \Phi(M_*)[h^3\text{Mpc}^{-3}/\log_{10} M_*]$			
	$0.1 < z < 0.35$	$0.35 < z < 0.55$	$0.55 < z < 0.75$	$0.75 < z < 1$
8.5	-1.310 ^{+0.095} _{-0.121}			
8.7	-1.351 ^{+0.087} _{-0.109}			
8.9	-1.440 ^{+0.100} _{-0.129}			
9.1	-1.433 ^{+0.078} _{-0.095}			
9.3	-1.558 ^{+0.077} _{-0.094}			
9.5	-1.619 ^{+0.071} _{-0.085}			
9.7	-1.627 ^{+0.067} _{-0.079}	-1.832 ^{+0.065} _{-0.077}		
9.9	-1.580 ^{+0.073} _{-0.088}	-1.885 ^{+0.041} _{-0.045}		
10.1	-1.649 ^{+0.085} _{-0.105}	-1.937 ^{+0.057} _{-0.065}		
10.3	-1.716 ^{+0.063} _{-0.074}	-1.912 ^{+0.059} _{-0.069}	-1.975 ^{+0.071} _{-0.085}	
10.5	-1.672 ^{+0.100} _{-0.130}	-1.953 ^{+0.081} _{-0.099}	-2.014 ^{+0.064} _{-0.075}	
10.7	-1.755 ^{+0.077} _{-0.093}	-1.967 ^{+0.072} _{-0.086}	-2.005 ^{+0.070} _{-0.083}	-2.252 ^{+0.068} _{-0.080}
10.9	-2.025 ^{+0.106} _{-0.141}	-2.096 ^{+0.066} _{-0.078}	-2.064 ^{+0.062} _{-0.073}	-2.273 ^{+0.064} _{-0.075}
11.1	-2.665 ^{+0.103} _{-0.136}	-2.375 ^{+0.082} _{-0.101}	-2.268 ^{+0.068} _{-0.082}	-2.376 ^{+0.091} _{-0.115}
11.3	-2.944 ^{+0.191} _{-0.348}	-2.793 ^{+0.109} _{-0.146}	-2.607 ^{+0.119} _{-0.165}	-2.670 ^{+0.094} _{-0.119}
11.5	-3.543 ^{+0.233} _{-0.538}	-3.443 ^{+0.178} _{-0.307}	-3.124 ^{+0.125} _{-0.175}	-3.034 ^{+0.185} _{-0.328}
11.7			-3.749 ^{+0.327} _{-3.698}	-3.489 ^{+0.415} _{-3.286}

Table C3. Measurements of projected 2PCF for the 20k zCOSMOS-bright sample.

r_p [Mpc/h]	$w_p(r_p)$			
	$9.5 < \log_{10} M_*^a < 10$	$10 < \log_{10} M_* < 10.5$	$10.5 < \log_{10} M_* < 11$	$\log_{10} M_* > 11$
$z = 0.1 - 0.4:$				
0.05	294.90 ± 189.05	355.72 ± 153.09		
0.08	73.82 ± 33.68	233.26 ± 83.15	210.96 ± 110.59	
0.13	127.43 ± 43.53	347.97 ± 185.17	438.21 ± 172.37	
0.20	133.53 ± 36.74	338.33 ± 147.38	310.01 ± 76.14	
0.32	71.94 ± 16.37	139.93 ± 30.13	170.42 ± 61.03	257.53 ± 236.69
0.51	57.09 ± 17.98	118.37 ± 38.55	120.22 ± 43.75	83.85 ± 101.63
0.81	47.63 ± 21.31	108.45 ± 34.08	109.02 ± 39.50	131.97 ± 91.14
1.29	24.18 ± 9.93	64.10 ± 26.90	55.22 ± 16.87	61.44 ± 34.57
2.05	16.17 ± 5.97	33.45 ± 12.66	44.44 ± 13.13	15.64 ± 17.03
3.24	20.22 ± 9.06	17.03 ± 10.12	33.52 ± 14.08	23.55 ± 18.33
5.15	20.37 ± 10.99	13.85 ± 9.56	21.59 ± 12.39	61.65 ± 45.37
8.15	16.77 ± 10.08	8.78 ± 5.70	21.25 ± 10.35	51.44 ± 66.49
12.92	15.08 ± 13.47	10.56 ± 10.82	17.22 ± 20.74	29.65 ± 45.99
$z = 0.4 - 0.7:$				
0.05	267.32 ± 159.39	287.06 ± 146.35	1050.60 ± 607.59	
0.08	194.03 ± 93.11	871.15 ± 398.37	225.57 ± 111.53	608.05 ± 625.92
0.13	310.61 ± 110.38	318.63 ± 110.40	410.82 ± 134.77	1422.62 ± 1046.69
0.20	70.68 ± 28.73	220.82 ± 85.55	324.08 ± 57.34	757.97 ± 383.36
0.32	61.18 ± 19.66	147.14 ± 34.25	206.05 ± 57.87	502.94 ± 185.45
0.51	68.66 ± 21.10	85.45 ± 26.50	93.68 ± 21.70	138.86 ± 82.74
0.81	47.87 ± 19.19	69.31 ± 24.37	75.58 ± 16.02	114.62 ± 79.28
1.29	31.29 ± 11.54	50.89 ± 17.23	73.07 ± 19.94	77.56 ± 56.18
2.05	22.25 ± 5.71	32.95 ± 10.61	55.80 ± 12.63	70.94 ± 57.34
3.24	19.59 ± 6.86	26.84 ± 10.77	34.85 ± 8.49	75.60 ± 58.57
5.15	18.51 ± 6.47	22.89 ± 10.41	34.32 ± 10.49	59.76 ± 23.38
8.15	15.49 ± 4.81	19.04 ± 6.90	28.59 ± 8.70	51.87 ± 34.94
12.92	11.97 ± 5.22	13.25 ± 6.51	20.30 ± 11.47	71.07 ± 75.47
$z = 0.7 - 1.0:$				
0.05		114.30 ± 164.73	339.04 ± 222.82	
0.08	286.91 ± 149.85	407.88 ± 215.06	649.25 ± 252.23	
0.13	32.47 ± 29.86	239.85 ± 143.83	685.55 ± 309.89	
0.20	172.30 ± 89.70	84.41 ± 29.88	505.32 ± 198.47	981.72 ± 929.88
0.32	2.15 ± 8.52	96.97 ± 40.72	178.41 ± 46.70	403.71 ± 259.99
0.51	42.51 ± 17.51	75.72 ± 21.27	240.45 ± 82.26	232.65 ± 101.66
0.81	57.62 ± 26.84	71.83 ± 25.75	149.32 ± 44.04	227.51 ± 147.96
1.29	32.41 ± 12.42	48.80 ± 15.11	89.28 ± 29.42	157.86 ± 64.45
2.05	37.93 ± 19.55	47.34 ± 14.98	103.07 ± 29.47	122.35 ± 48.98
3.24	20.63 ± 10.82	37.11 ± 11.57	69.40 ± 18.87	84.49 ± 36.11
5.15	25.55 ± 15.90	24.75 ± 8.61	58.74 ± 17.32	77.43 ± 35.61
8.15	15.79 ± 11.78	21.18 ± 9.08	34.89 ± 13.73	45.78 ± 26.28
12.92	14.50 ± 11.94	15.42 ± 9.78	17.03 ± 7.42	24.26 ± 16.76

^a The unit of M_* is M_\odot .